

Branch structure and nonextensive thermodynamics of Kalb-Ramond-ModMax black holes: observational signatures

Erdem Sucu ,^{1,*} İzzet Sakalli ,^{1,†} and Emmanuel N. Saridakis ,^{2,3,4,‡}

¹*Physics Department, Eastern Mediterranean University, 99628, Famagusta, Cyprus*
²*Institute for Astronomy, Astrophysics, Space Applications and Remote Sensing, National Observatory of Athens, 15236 Penteli, Greece*

³*Departamento de Matemáticas, Universidad Católica del Norte, Avda. Angamos 0610, Casilla 1280 Antofagasta, Chile*

⁴*Department of Astronomy, School of Physical Sciences, University of Science and Technology of China, Hefei 230026, P.R. China*

We investigate a static, spherically symmetric black hole arising in Einstein gravity coupled to a Kalb-Ramond field and ModMax nonlinear electrodynamics, both of which are independently well motivated extensions of standard electrovacuum gravity. The solution depends, beyond mass and charge, on a Lorentz-violating parameter, a ModMax deformation parameter, and a discrete branch selector $\zeta = \pm 1$. We show that the ordinary branch admits extremal and non-extremal configurations, while the phantom branch generically supports a single-horizon geometry. Black-hole thermodynamics is analyzed within the Tsallis non-extensive framework, revealing branch-dependent stability and Joule-Thomson behavior. Weak gravitational lensing, photon propagation in plasma, and tidal forces are then studied, revealing clear optical and strong-field signatures that distinguish the two branches. In particular, the ordinary branch exhibits finite-radius tidal inversion, absent in the phantom sector. Our results demonstrate that the combined Kalb-Ramond and ModMax effects lead to a rich and observationally distinguishable black-hole phenomenology.

I. INTRODUCTION

Black holes (BHs) occupy a central position in modern theoretical physics, providing a unique arena where gravity, quantum field theory, and high-energy physics intersect [1, 2]. Within General Relativity (GR), the Schwarzschild and Reissner-Nordström (RN) solutions constitute the canonical descriptions of neutral and electrically charged BHs, respectively. Nevertheless, both theoretical considerations related to quantum gravity and a growing body of observational evidence from cosmology and astrophysics motivate the exploration of gravitational frameworks that extend or modify GR [3, 4]. Such extensions often introduce additional fields, nonlinearities, or symmetry-breaking mechanisms, leading to nontrivial modifications of the causal structure, thermodynamics, and optical properties of BH spacetimes [5–10].

Among the most theoretically well-motivated extensions are those inspired by string theory and its low-energy effective descriptions. In this context, the Kalb-Ramond (KR) field, a rank-two antisymmetric tensor arising naturally in the bosonic and heterotic string spectra, provides a concrete realization of new gravitational degrees of freedom [11–13]. The associated three-form field strength can be interpreted either as spacetime torsion or as a vacuum condensate inducing Lorentz symmetry breaking (LSB) in the gravitational sector [14, 15]. When

coupled to Einstein gravity, the KR background modifies the spacetime geometry through an effective parameter ℓ that rescales the asymptotic structure while preserving spherical symmetry. The resulting BH geometries exhibit horizon and thermodynamic properties that differ from their GR counterparts, rendering them suitable probes of string-inspired effects in the strong-field regime [16, 17].

In parallel, nonlinear electrodynamics (NED) has emerged as a powerful framework for addressing strong-field phenomena in gauge theories coupled to gravity [18, 19]. Beyond the classic Born-Infeld construction [18], recent attention has focused on ModMax electrodynamics, which constitutes the unique one-parameter deformation of Maxwell theory preserving both conformal invariance and electric-magnetic duality [20, 21]. The ModMax Lagrangian introduces a dimensionless parameter γ that interpolates continuously between the Maxwell limit and a genuinely nonlinear regime. When minimally coupled to gravity, ModMax electrodynamics gives rise to BH solutions with modified charge contributions and novel horizon structures [20, 22]. A distinctive feature of this theory is the emergence of two mathematically consistent branches: an ordinary branch ($\zeta = +1$), continuously connected to the RN geometry, and a phantom branch ($\zeta = -1$), in which the electromagnetic energy density effectively reverses sign, leading to qualitatively different physical behavior [23].

The combined presence of LSB effects and nonlinear electromagnetic dynamics provides a particularly rich setting for BH physics [24, 25]. In the Einstein-KR-ModMax framework, the spacetime geometry is controlled jointly by three deformation parameters: the KR parameter ℓ , the ModMax nonlinearity parameter γ , and the branch selector ζ . This interplay gener-

* 23600348@emu.edu.tr

† izzet.sakalli@emu.edu.tr

‡ msaridak@noa.gr

ates BH solutions with rescaled asymptotics, branch-dependent horizon structures, and modified thermodynamic and optical properties that distinguish them from both Schwarzschild and RN geometries [26]. Understanding how these different modifications combine and manifest in physical observables is essential for assessing their phenomenological relevance.

Black hole thermodynamics offers a particularly sensitive probe of the underlying gravitational dynamics. Since the formulation of the laws of BH mechanics and the discovery of Hawking radiation [27, 28], thermodynamic considerations have provided deep insights into the interplay between gravity, quantum theory, and statistical mechanics. However, the standard Boltzmann-Gibbs framework may be inadequate for gravitational systems characterized by long-range interactions and strong correlations [29, 30]. Non-extensive generalizations, most notably Tsallis entropy, introduce a deformation parameter δ that quantifies deviations from the area law and can significantly modify the thermodynamic behavior of BHs [29, 31, 32]. Within this framework, quantities such as internal energy, free energy, pressure, and heat capacity acquire nontrivial corrections, potentially altering phase structure and stability [33–35]. The Joule-Thomson (JT) expansion further enriches this picture by providing a diagnostic of heating-cooling transitions in extended thermodynamic space [36–39].

On the observational side, gravitational lensing remains one of the most direct probes of spacetime geometry in the strong-field regime. Since its first experimental confirmation [40], lensing has evolved into a precision tool for testing GR and constraining alternative theories [41]. The Gauss-Bonnet (GB) approach [42, 43] offers a coordinate-independent method for computing weak-field deflection angles and has been widely applied in BH spacetimes [44–48]. Moreover, realistic astrophysical environments are typically permeated by plasma, which modifies photon propagation through dispersive effects. In such settings, the photon sphere and shadow properties depend not only on the spacetime geometry but also on the plasma distribution, providing additional discriminants among competing gravitational models [49–51].

Tidal forces constitute a complementary probe of the strong-field regime. Through the geodesic deviation equation, tidal effects encode local curvature information and govern the deformation of extended bodies approaching a BH [52, 53]. In modified gravity scenarios, tidal force profiles may deviate substantially from the Schwarzschild case, potentially exhibiting enhanced magnitudes or sign reversals that influence tidal disruption processes [54–56].

Motivated by these considerations, in this work we perform a systematic investigation of Kalb-Ramond-ModMax BHs across both their ordinary and phantom branches. We analyze the spacetime structure and thermodynamics within the Tsallis entropy framework, including the JT expansion, and explore optical signatures

through weak gravitational lensing and photon propagation in plasma environments. Finally, we examine tidal forces and identify branch-dependent features, including the conditions under which tidal inversion may occur. By combining geometric, thermodynamic, and observational diagnostics within a unified setting, we aim to clarify the physical implications of branch structure and non-extensive effects, and to identify signatures that could distinguish these BHs from standard GR solutions and other modified gravity models.

The paper is organized as follows. In Section II we present the KR-ModMax black hole solution, analyze its branch-dependent horizon structure, and derive the Hawking temperature. Section III develops the non-extensive thermodynamic description based on Tsallis entropy, while the Joule-Thomson expansion is examined in Section IV. In Section V we discuss the weak gravitational lensing and vacuum photon-sphere properties. Plasma effects on photon propagation and their impact on photon spheres are analyzed separately in Section VI. In Section VII we investigate tidal forces and branch-dependent deformations. Finally, Section VIII summarizes our results and outlines future directions.

II. KR-MODMAX BH SOLUTION AND HORIZON STRUCTURE

We begin by introducing the gravitational setup and exact black hole solution arising from the combined presence of a Kalb-Ramond background and ModMax nonlinear electrodynamics. Particular emphasis is placed on the emergence of a branch structure, which plays a central role in shaping the causal, thermodynamic, and observational properties analyzed in subsequent sections.

A. Field equations, exact solution, and horizon structure

We consider static and spherically symmetric black hole geometries arising from Einstein gravity coupled simultaneously to a Kalb-Ramond (KR) three-form condensate and ModMax nonlinear electrodynamics. This framework combines Lorentz symmetry breaking (LSB) effects of string-theoretic origin with the unique conformally invariant deformation of Maxwell theory [20, 57, 58]. Owing to spherical symmetry, the spacetime metric can be written in the standard form

$$ds^2 = -f(r) dt^2 + \frac{dr^2}{f(r)} + r^2 d\Omega^2, \quad (1)$$

where all geometric information is encoded in the lapse function $f(r)$, which captures both the KR-induced vacuum deformation and the nonlinear electromagnetic corrections [12, 59]. The Einstein equations, supplemented by the modified Maxwell sector, reduce to a single ordinary differential equation for $f(r)$.

The KR field originates from an antisymmetric rank-two tensor $B_{\mu\nu}$ appearing in the massless sector of bosonic string theory. A nonvanishing condensate of its associated three-form field strength induces spontaneous breaking of local Lorentz invariance and rescales the effective gravitational and electromagnetic couplings through a dimensionless parameter ℓ [60, 61]. Moreover, ModMax electrodynamics constitutes the unique one-parameter nonlinear extension of Maxwell theory that preserves both conformal invariance and electromagnetic duality [20, 62]. The deviation from linear electrodynamics is governed by the parameter γ , with the Maxwell limit recovered as $\gamma \rightarrow 0$.

In this setting, the modified Maxwell equations admit a purely radial electric field configuration $\Phi = \Phi(r)$, constrained by charge conservation. Direct integration yields the electrostatic potential

$$\Phi(r) = \frac{Q e^{-\gamma}}{(1 - \ell) r}, \quad (2)$$

where the factor $(1 - \ell)^{-1}$ reflects the KR-induced rescaling of the effective electric coupling. Substituting Eq. (2) into the gravitational field equations and imposing asymptotic flatness leads to the exact metric function [57]

$$f(r) = \frac{1}{1 - \ell} - \frac{2M}{r} + \frac{\zeta Q^2 e^{-\gamma}}{(1 - \ell)^2 r^2}, \quad (3)$$

where M is the ADM mass, Q the electric charge, and $\zeta = \pm 1$ distinguishes between the ordinary ($\zeta = +1$) and phantom ($\zeta = -1$) branches of ModMax electrodynamics. While the ordinary branch corresponds to a positive electromagnetic energy density and continuously connects to the Reissner-Nordström solution, the phantom branch reverses the sign of the electromagnetic stress-energy contribution, leading to qualitatively different gravitational behavior.

The asymptotic structure of the spacetime follows from

$$\lim_{r \rightarrow \infty} f(r) = \frac{1}{1 - \ell}, \quad (4)$$

which shows that the KR parameter ℓ modifies the normalization of the timelike Killing vector at infinity. For $\ell < 1$, the geometry remains asymptotically flat up to this constant rescaling, preserving the standard $1/r$ falloff of curvature invariants. Equivalently, the effective gravitational coupling is renormalized according to $G_{\text{eff}} = G/(1 - \ell)$, with direct implications for orbital dynamics and gravitational lensing observables [61, 63].

In Fig. 1 we display the radial profile of the metric function $f(r)$ for four representative configurations. In particular, panel (a) illustrates the ordinary branch at fixed $(\ell, \gamma) = (0.5, 2.0)$: as Q increases from 0.3 to 1.3, the solution transitions from a non-extremal BH with two distinct horizons, through the extremal configuration at $Q \approx 0.93$, to a naked singularity for $Q \geq 1.0$.

Panel (b) presents the phantom branch under identical KR-ModMax parameters, where all curves intersect the $f = 0$ axis exactly once, confirming the single-horizon topology. Finally, panels (c) and (d) examine the sensitivity to ℓ and γ respectively, demonstrating how these parameters shift horizon locations and modify the near-horizon geometry.

B. Branch dichotomy and physical interpretation

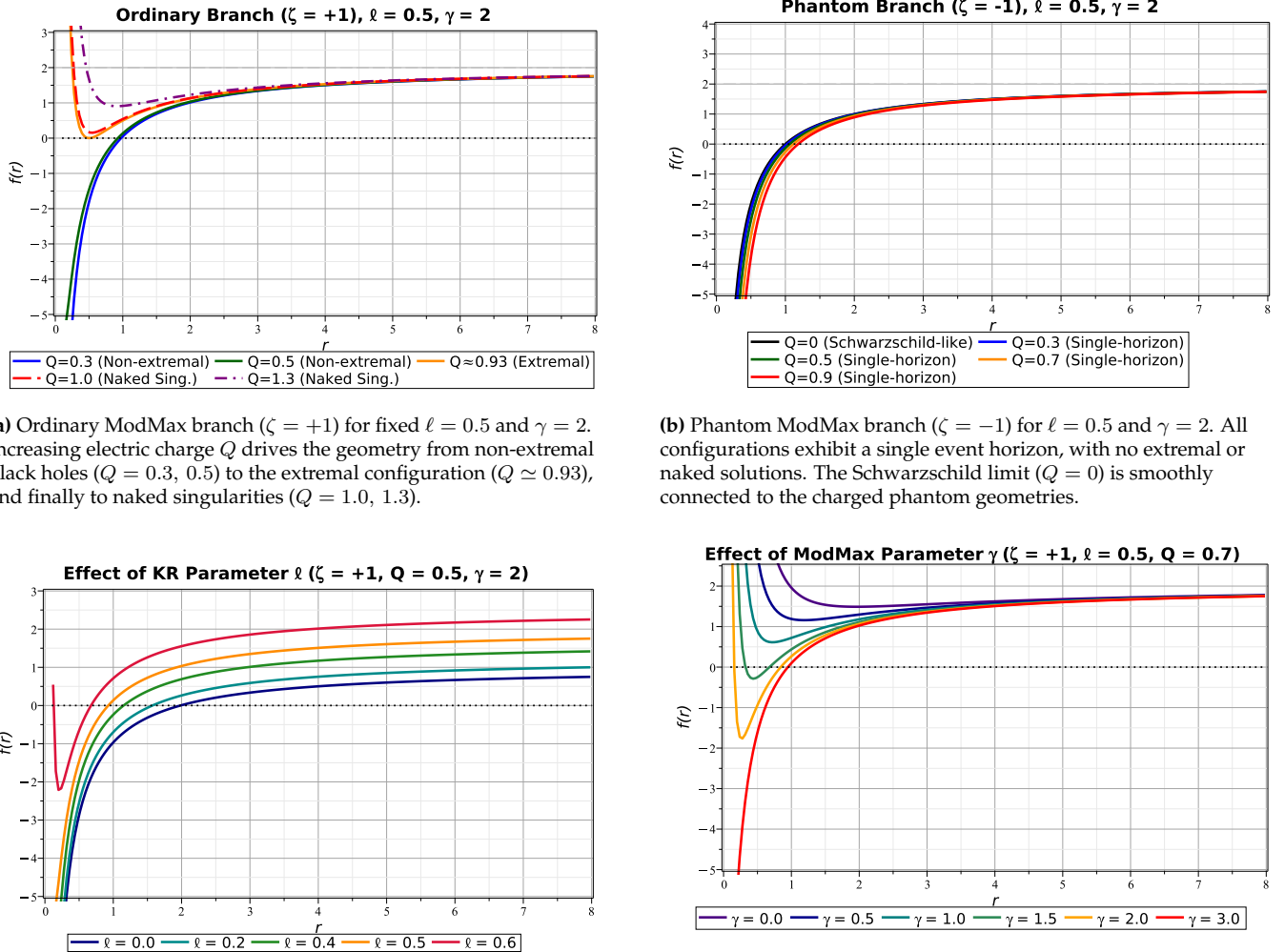
A distinctive feature of the Kalb-Ramond-ModMax black hole solution is the existence of two mathematically consistent branches, labeled by $\zeta = \pm 1$, which lead to qualitatively different spacetime structures and physical behavior. This branch dichotomy originates from the nonlinear electromagnetic sector and persists even in the presence of the Kalb-Ramond deformation, playing a central role in shaping the properties of the solution.

For the ordinary branch ($\zeta = +1$), the electromagnetic contribution partially counteracts the gravitational attraction, closely resembling the behavior familiar from the Reissner-Nordström geometry. As the electric charge approaches a critical value, the event and Cauchy horizons merge and the black hole reaches an extremal configuration with vanishing Hawking temperature. This limit is associated with the emergence of a degenerate horizon and signals a qualitative change in the near-horizon geometry. For larger charge values, the solution admits no horizons, giving rise to naked singularities.

On the other hand, the phantom branch ($\zeta = -1$) exhibits a markedly different structure. In this case, the effective electromagnetic contribution reinforces the gravitational field, eliminating the possibility of extremal configurations altogether. The spacetime admits a single event horizon for all values of the charge, and the Hawking temperature remains strictly positive throughout the parameter space. This absence of inner horizons implies a simpler causal structure and avoids the Cauchy horizon instabilities that typically afflict charged black holes in GR-like settings.

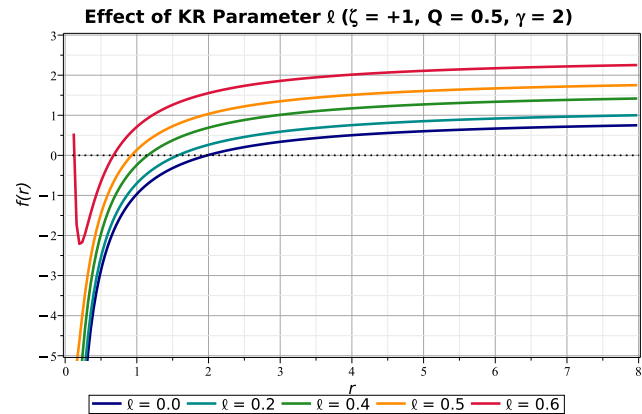
These geometric differences have direct physical implications. The reinforced gravitational potential characterizing the phantom branch modifies the location of the photon sphere and affects null geodesic propagation, while the ordinary branch retains features continuously connected to the Reissner-Nordström case. Similarly, the distinct horizon structures lead to different thermodynamic behavior, particularly near extremality, and influence tidal effects experienced by infalling matter. A geometric visualization of the equatorial spatial geometry, illustrating the single-horizon topology of the phantom branch, is presented in Appendix A.

The coexistence of ordinary and phantom branches within the same theoretical framework naturally raises the question of physical viability and observational discrimination. While the ordinary branch admits a smooth GR limit as $\ell \rightarrow 0$ and $\gamma \rightarrow 0$, the phantom branch repre-



(a) Ordinary ModMax branch ($\zeta = +1$) for fixed $\ell = 0.5$ and $\gamma = 2$. Increasing electric charge Q drives the geometry from non-extremal black holes ($Q = 0.3, 0.5$) to the extremal configuration ($Q \simeq 0.93$), and finally to naked singularities ($Q = 1.0, 1.3$).

(b) Phantom ModMax branch ($\zeta = -1$) for $\ell = 0.5$ and $\gamma = 2$. All configurations exhibit a single event horizon, with no extremal or naked solutions. The Schwarzschild limit ($Q = 0$) is smoothly connected to the charged phantom geometries.



(c) Effect of the Kalb-Ramond parameter ℓ on the ordinary branch ($\zeta = +1, Q = 0.5, \gamma = 2$). Increasing ℓ shifts the event horizon inward and enhances the asymptotic normalization $f_\infty = (1 - \ell)^{-1}$.

FIG. 1: Metric function $f(r)$ for KR-ModMax black holes in the ordinary ($\zeta = +1$) and phantom ($\zeta = -1$) branches. The horizontal dashed line $f(r) = 0$ marks the locations of event horizons. Panel (a) illustrates the charge-driven transition from non-extremal to extremal and naked configurations in the ordinary branch. Panel (b) demonstrates the absence of extremal or naked solutions in the phantom sector. Panels (c) and (d) display the sensitivity of the geometry to the Kalb-Ramond parameter ℓ and the ModMax parameter γ , respectively.

sents a genuinely novel class of solutions with no direct counterpart in standard Einstein-Maxwell theory. In the following sections, we explore how this branch structure manifests in thermodynamic properties, optical signatures, and tidal forces, and assess whether these effects can provide meaningful criteria for distinguishing between the two branches.

C. Hawking temperature

The stationarity of the Kalb-Ramond-ModMax black hole spacetime ensures the existence of a timelike Killing

vector associated with time translations,

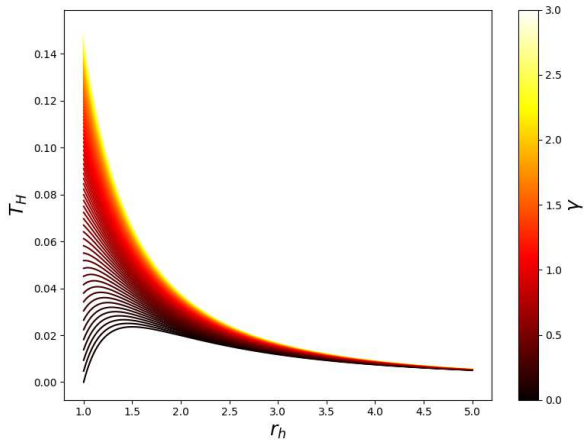
$$\xi^\mu = \left(\frac{\partial}{\partial t} \right)^\mu, \quad (5)$$

which gives rise to a conserved energy along timelike and null geodesics [28]. The surface gravity κ , characterizing the strength of the gravitational field at the event horizon, is defined through the Killing identity

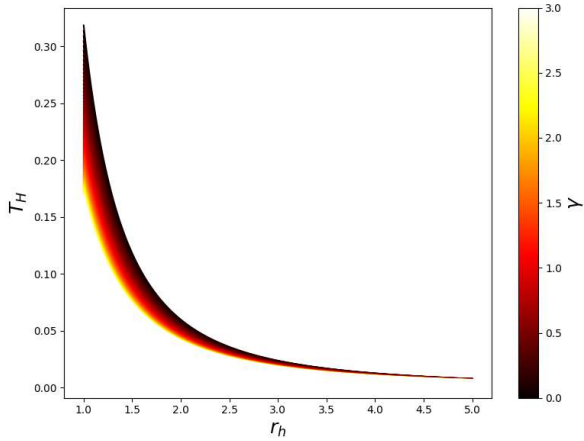
$$\nabla_\nu (\xi^\mu \xi_\mu) = -2 \kappa \xi_\nu, \quad (6)$$

and remains constant over the horizon in accordance with the zeroth law of black hole mechanics [27, 64].

For the static metric function (3), the surface gravity is obtained directly from the radial derivative of the lapse



(a) Ordinary ModMax branch ($\zeta = +1$). The electromagnetic contribution suppresses the Hawking temperature, producing Reissner-Nordström-like behavior. For small γ (dark curves), T_H approaches zero at finite r_h , signaling the onset of extremality. Increasing γ exponentially weakens the effective charge through $e^{-\gamma}$, shifting the temperature curves upward and reducing the extremal horizon radius.



(b) Phantom ModMax branch ($\zeta = -1$). The sign-reversed electromagnetic sector enhances the Hawking temperature uniformly. All configurations remain strictly nonzero, precluding extremal limits. The temperature reaches $T_H \simeq 0.32$ at small r_h , approximately twice the maximum attained in the ordinary branch, reflecting reinforced thermal emission.

FIG. 2: Hawking temperature T_H as a function of the horizon radius r_h for KR-ModMax black holes with fixed parameters $M = 1.0$, $Q = 0.5$, and $\ell = 0.5$. The color scale denotes the ModMax parameter $\gamma \in [0, 3]$. The ordinary branch exhibits a γ -dependent approach to extremality, whereas the phantom branch maintains strictly positive temperature throughout the entire parameter space.

function evaluated at the outer horizon radius r_+ ,

$$\kappa = \frac{1}{2} f'(r) \Big|_{r=r_+} = \frac{M}{r_+^2} - \frac{\zeta Q^2 e^{-\gamma}}{(1-\ell)^2 r_+^3}. \quad (7)$$

The relative sign of the two terms is controlled by the

branch parameter ζ , leading to qualitatively different thermal behavior in the ordinary and phantom branches.

Quantum particle production near the event horizon results in Hawking radiation, with temperature measured by asymptotic observers given by $T_H = \kappa/(2\pi)$ [28]. For the present geometry, this yields

$$T_H = \frac{M}{2\pi r_+^2} - \frac{\zeta Q^2 e^{-\gamma}}{2\pi(1-\ell)^2 r_+^3}. \quad (8)$$

This expression shows the combined influence of the Kalb-Ramond background, which rescales the effective couplings through $(1-\ell)^{-2}$, and the ModMax nonlinear electrodynamics, whose contribution is suppressed by the factor $e^{-\gamma}$ and whose sign is determined by ζ .

In the ordinary branch ($\zeta = +1$), the electromagnetic contribution counteracts the gravitational term, closely mirroring the behavior of the Reissner-Nordström black hole. As the charge approaches the critical value $Q_{\text{ext}} = M\sqrt{(1-\ell)^3 e^\gamma}$, the Hawking temperature vanishes and the horizons coincide, signaling the onset of an extremal configuration with degenerate surface gravity. This limit is associated with a qualitative change in the near-horizon geometry and marks the boundary of the semiclassical description [65, 66].

The phantom branch ($\zeta = -1$) exhibits a markedly different thermal structure. In this case, the electromagnetic term reinforces the gravitational contribution, leading to systematically higher temperatures and precluding the existence of extremal configurations. The Hawking temperature remains strictly positive throughout the parameter space, in agreement with the single-horizon causal structure discussed in the previous subsection.

The branch-dependent behavior of the Hawking temperature is illustrated in Fig. 2, where T_H is shown as a function of the horizon radius for representative values of the ModMax parameter γ . In the ordinary branch [Fig. 2a], increasing γ suppresses the effective charge contribution and progressively restores Schwarzschild-like behavior. By contrast, in the phantom branch [Fig. 2b], the temperature curves are shifted upward and exhibit a smoother dependence on γ , reflecting the absence of extremality.

Table I summarizes the resulting horizon structure across representative parameter combinations for both branches, explicitly illustrating the transition between non-extremal, extremal, and horizonless configurations. The numerical values reported in Table I are fully consistent with the aforementioned trends and further reveal the enhanced thermal robustness of the phantom branch against charge variations.

III. TSALLIS ENTROPY AND KR-MODMAX BH THERMODYNAMICS

Black hole thermodynamics provides a sensitive probe of the microscopic structure of gravitational theories. In

TABLE I: Horizon structure of KR-ModMax black holes with $M = 1$. The ordinary branch ($\zeta = +1$) exhibits non-extremal, near-extremal, and naked singularity configurations depending on Q relative to $Q_{\text{ext}} = M\sqrt{(1-\ell)^3 e^\gamma}$. The phantom branch ($\zeta = -1$) admits only single-horizon black holes with r_+ increasing monotonically with charge. Configurations marked with † correspond to the 3D embedding diagrams of Fig. 12 of Appendix A. Here r_\pm denote outer/inner horizon radii and T_H is the Hawking temperature.

ζ	ℓ	γ	Q	r_+	r_-	T_H	Classification
Ordinary Branch ($\zeta = +1$) – Fig. 1a							
+1	0.5	2.0	0.3	0.975	0.025	0.159	Non-extremal BH
+1	0.5	2.0	0.5	0.927	0.073	0.158	Non-extremal BH
+1	0.5	2.0	0.7	0.843	0.157	0.154	Non-extremal BH
+1	0.5	2.0	0.9	0.675	0.325	0.122	Near-extremal BH
+1	0.5	2.0	1.0	–	–	–	Naked Singularity
+1	0.5	2.0	1.3	–	–	–	Naked Singularity
Effect of KR Parameter ℓ ($\zeta = +1, Q = 0.5, \gamma = 2$) – Fig. 1c							
+1	0.0	2.0	0.5	1.983	0.017	0.040	Non-extremal BH
+1	0.2	2.0	0.5	1.573	0.027	0.062	Non-extremal BH
+1	0.4	2.0	0.5	1.151	0.049	0.110	Non-extremal BH
+1	0.5	2.0	0.5	0.927	0.073	0.158	Non-extremal BH
Effect of ModMax Parameter γ ($\zeta = +1, \ell = 0.5, Q = 0.7$) – Fig. 1d							
+1	0.5	0.0	0.7	–	–	–	Naked Singularity
+1	0.5	1.0	0.7	–	–	–	Naked Singularity
+1	0.5	2.0	0.7	0.843	0.157	0.154	Non-extremal BH
+1	0.5	3.0	0.7	0.912	0.088	0.157	Non-extremal BH
Phantom Branch ($\zeta = -1$) – Fig. 1b							
-1	0.5	2.0	0.0	1.000	–	0.159	Single-horizon BH
-1	0.5	2.0	0.3	1.024	–	0.159	Single-horizon BH
-1	0.5	2.0	0.5	1.064	–	0.159	Single-horizon BH
-1	0.5	2.0	0.7	1.119	–	0.157	Single-horizon BH
-1	0.5	2.0	0.9	1.185	–	0.155	Single-horizon BH
3D Embedding Configurations ($\zeta = -1$) – Fig. 12							
-1^\dagger	0.2	0.5	0.2	1.62	–	0.062	Single-horizon BH
-1^\dagger	0.5	3.0	0.5	1.02	–	0.159	Single-horizon BH
-1^\dagger	0.7	1.0	0.8	1.24	–	0.104	Single-horizon BH
-1^\dagger	0.4	2.0	0.1	1.20	–	0.110	Single-horizon BH

the presence of nonlinear matter sectors and Lorentz symmetry breaking backgrounds, departures from standard extensive thermodynamics may naturally arise. In this section, we adopt a non-extensive framework based on Tsallis entropy in order to examine how such effects modify the thermodynamic behavior of Kalb-Ramond-ModMax black holes and how the resulting properties depend on the underlying branch structure.

A. Tsallis entropy, internal energy, and free energy

Within the Tsallis framework, the entropy of a black hole with event-horizon radius r_h is taken to be [29]

$$S_T = (\pi r_h^2)^\delta, \quad (9)$$

where δ denotes the non-extensivity parameter. The standard Bekenstein-Hawking entropy $S_{\text{BkH}} = \pi r_h^2$ (in units $G = \hbar = c = k_B = 1$) is recovered for $\delta = 1$ [28, 67]. Values $\delta \neq 1$ encode deviations from extensivity, reflecting

the possible presence of long-range correlations, horizon fluctuations, or an underlying fractal microstructure associated with quantum gravitational effects [68]. In what follows, we focus on $\delta \geq 1$, which ensures physical behavior and avoids pathological divergences.

The internal energy associated with the Tsallis entropy is obtained from the first law of black hole thermodynamics,

$$E_T = \int T_H dS_T, \quad (10)$$

where the non-extensive nature of the entropy introduces a δ -dependent weighting through $dS_T/dr_h = 2\delta \pi^\delta r_h^{2\delta-1}$. Substituting the Hawking temperature given in Eq. (8) and performing the integration yields

$$E_T = \frac{\mathcal{A}}{2r_h^3(1-\ell)^2 e^\gamma \pi (2\delta-1)(4\delta-3)}, \quad (11)$$

with the numerator

$$\begin{aligned} \mathcal{A} = \delta r_h^{4\delta} \pi^{2\delta} & \left[4M e^\gamma \delta \ell^2 r_h - 8M e^\gamma \delta \ell r_h \right. \\ & - 3M e^\gamma \ell^2 r_h + 4M e^\gamma \delta r_h + 6M e^\gamma \ell r_h \\ & \left. - 3M e^\gamma r_h - 4Q^2 \delta \zeta + 2\zeta Q^2 \right]. \end{aligned} \quad (12)$$

The denominators $(2\delta-1)$ and $(4\delta-3)$ formally signal divergences at $\delta = 1/2$ and $\delta = 3/4$, respectively, however these values lie outside the physically relevant regime considered here.

The behavior of the internal energy as a function of the horizon radius and the non-extensivity parameter is illustrated in Fig. 3 for both ModMax branches. In the ordinary branch (Fig. 3a), E_T increases monotonically with r_h and δ , reflecting the standard competition between gravitational and electromagnetic contributions. In the phantom branch (Fig. 3b), the internal energy exhibits a similar qualitative dependence but is systematically enhanced. This increase originates from the sign reversal $\zeta = -1$, which effectively converts the electromagnetic contribution into an additional heating source, leading to a larger accumulated thermal energy for fixed horizon size.

A complementary thermodynamic quantity is the Helmholtz free energy, which characterizes the maximum extractable work at fixed temperature and provides insight into global stability. Within the Tsallis framework, it is obtained through the Legendre transformation

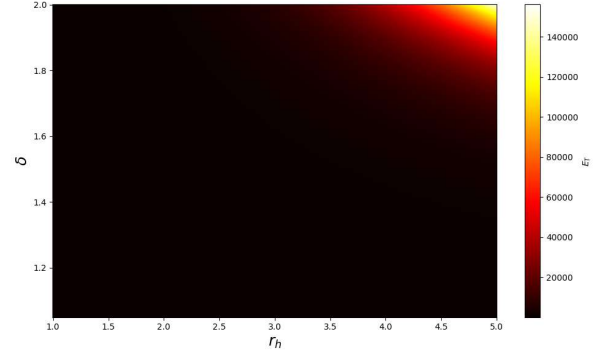
$$F_T = - \int S_T dT_H. \quad (13)$$

Performing the integration yields

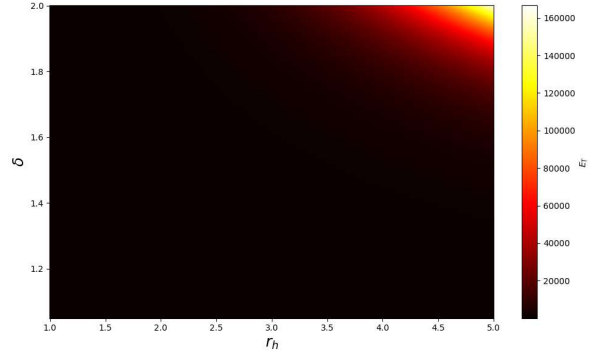
$$F_T = \frac{\mathcal{K}}{r_h^3(1-\ell)^2 \pi (2\delta-1)(4\delta-3)}, \quad (14)$$

where

$$\mathcal{K} = (1-\ell)^2 \left(\delta - \frac{3}{4} \right) \pi^{2\delta} M r_h^{4\delta+1}$$



(a) Ordinary ModMax branch ($\zeta = +1$). The Tsallis internal energy E_T increases monotonically with the horizon radius r_h , displaying smooth scaling across the non-extensivity range $\delta \in [1, 2]$. Charge effects suppress the short-distance contribution, leading to a gradual approach toward Schwarzschild-KR behaviour at large radii.

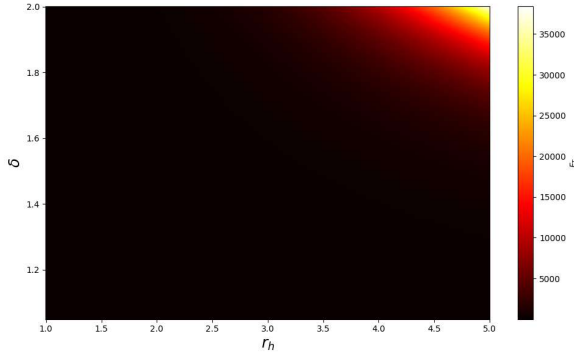


(b) Phantom ModMax branch ($\zeta = -1$). The internal energy exhibits systematically steeper growth compared to the ordinary branch. The sign-reversed electromagnetic sector amplifies the near-horizon contribution, enhancing both the magnitude of E_T and its sensitivity to the non-extensivity parameter δ .

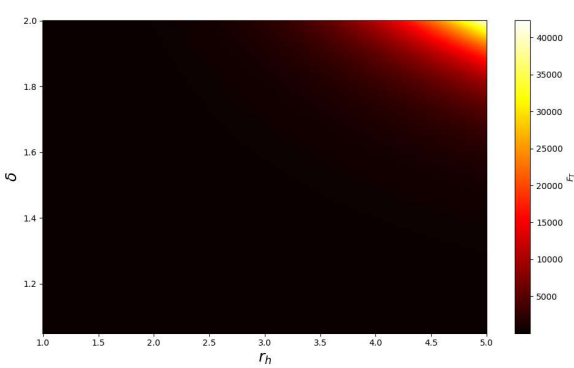
FIG. 3: Tsallis internal energy E_T as a function of the horizon radius r_h for KR-ModMax black holes with fixed parameters $M = 1.0$, $Q = 0.5$, $\ell = 0.5$, and $\gamma = 2.0$. The color scale denotes the non-extensivity parameter $\delta \in [1, 2]$. Across the entire parameter space, the phantom branch maintains higher internal energy, establishing a clear thermodynamic hierarchy between the two ModMax sectors.

$$\begin{aligned} - \left(\delta - \frac{1}{2} \right) & \left[(4\delta-3) (-4\zeta Q^2 e^{-\gamma} + 4Mr_h(1-\ell)^2) \right. \\ & \left. + \frac{3e^{-\gamma} \pi^{2\delta} r_h^{4\delta} Q^2 \zeta}{2} \right]. \end{aligned} \quad (15)$$

The behavior of the Helmholtz free energy is displayed in Fig. 4. In the ordinary branch, F_T decreases monotonically with the horizon radius, with increasing δ enhancing the preference for larger, thermodynamically stable configurations. In the phantom branch, the free energy



(a) Ordinary ModMax branch ($\zeta = +1$). The Tsallis Helmholtz free energy F_T decreases monotonically with increasing horizon radius r_h , approaching zero asymptotically. Larger non-extensivity parameter δ deepens the free-energy well at small r_h , indicating a higher thermodynamic cost for compact configurations and a tendency toward instability near the horizon.



(b) Phantom ModMax branch ($\zeta = -1$). The free energy attains systematically larger magnitudes at small r_h and exhibits a steeper radial dependence. The enhanced separation between δ -curves reflects a stronger sensitivity to non-extensive corrections, signaling a more pronounced thermodynamic instability in the phantom sector.

FIG. 4: Tsallis Helmholtz free energy F_T as a function of the horizon radius r_h for KR-ModMax black holes with the same parameters as Fig. 3. While both branches show monotonic decay with increasing r_h , the phantom branch maintains a larger free-energy magnitude throughout, reinforcing the thermodynamic hierarchy inferred from the internal energy and anticipating the branch-dependent stability behavior discussed in subsequent sections.

exhibits a similar qualitative trend but with systematically larger magnitude and steeper descent, indicating that non-extensive effects couple more strongly when the electromagnetic contribution reinforces the gravitational field [69].

B. Thermodynamic pressure and equation of state

In the extended formulation of black hole thermodynamics, macroscopic thermodynamic variables can be introduced through appropriate conjugate pairs, allowing one to explore phase structure beyond the standard entropy-temperature description [70]. Within the present Tsallis framework, we define an effective thermodynamic pressure through the Helmholtz free energy, while retaining the geometric interpretation of the thermodynamic volume as

$$V = \frac{4\pi r_h^3}{3}. \quad (16)$$

The pressure is then obtained as

$$P_T = -\frac{\partial F_T}{\partial V}, \quad (17)$$

which encodes how non-extensive effects and matter-sector modifications reshape the effective equation of state. Hence, carrying out the differentiation yields

$$P_T = \frac{\mathcal{D}}{16(1-\ell)^2 r_h^6 \pi^2}, \quad (18)$$

with

$$\mathcal{D} = -2M\pi^{2\delta}(1-\ell)^2 r_h^{4\delta+1} + 3e^{-\gamma}\pi^{2\delta} r_h^{4\delta} Q^2 \zeta + 6\zeta Q^2 e^{-\gamma} - 4Mr_h(1-\ell)^2. \quad (19)$$

As we can see, the resulting pressure is negative throughout the parameter space, reflecting the attractive nature of the effective interaction governing the black hole thermodynamics in this setting.

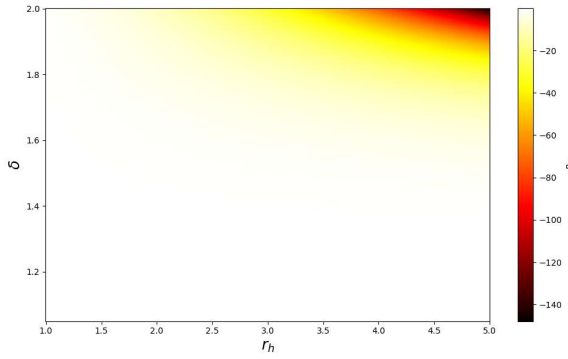
The behavior of P_T as a function of the horizon radius is illustrated in Fig. 5. In the ordinary branch (Fig. 5a), the pressure decreases smoothly in magnitude as r_h increases, with larger values of the non-extensivity parameter δ systematically reducing the absolute pressure. In the phantom branch (Fig. 5b), a similar qualitative trend is observed, although the magnitude of the pressure decreases more rapidly at small horizon radii, reflecting the enhanced role of the electromagnetic contribution when $\zeta = -1$. At sufficiently large r_h , both branches converge as the mass term dominates over charge-dependent corrections.

This effective equation of state provides the thermodynamic background for the Joule-Thomson expansion discussed in the following section, where heating and cooling regimes are analyzed in terms of the response of the Hawking temperature to pressure variations.

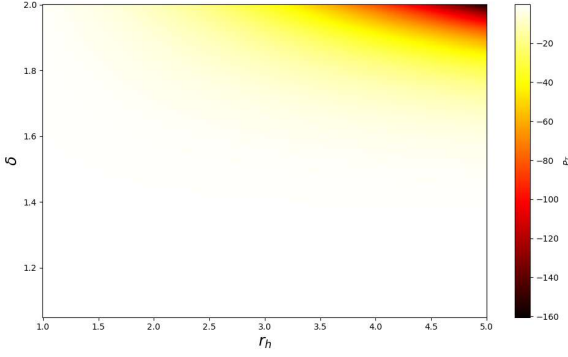
C. Heat capacity and local stability

Local thermodynamic stability of the black hole is determined by the heat capacity at constant volume, defined as

$$C_V = T_H \left(\frac{\partial S_T}{\partial T_H} \right)_V, \quad (20)$$



(a) Ordinary ModMax branch ($\zeta = +1$). The Tsallis thermodynamic pressure P_T remains negative throughout the explored parameter space and decreases smoothly with increasing horizon radius r_h . Larger non-extensivity parameter δ uniformly reduces the pressure magnitude, indicating that non-extensive entropy softens the effective equation of state and moderates the response to horizon shrinkage.

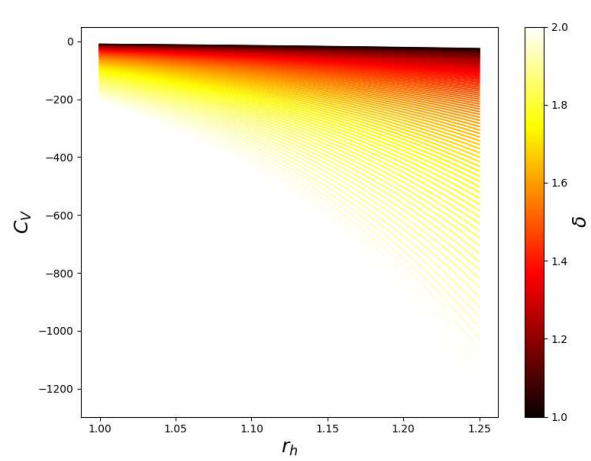


(b) Phantom ModMax branch ($\zeta = -1$). The pressure exhibits a similar negative range but displays a steeper radial dependence at small r_h . The sign-reversed electromagnetic sector enhances the sensitivity of P_T to near-horizon physics, foreshadowing stronger branch dependence in pressure-driven processes such as Joule-Thomson expansion.

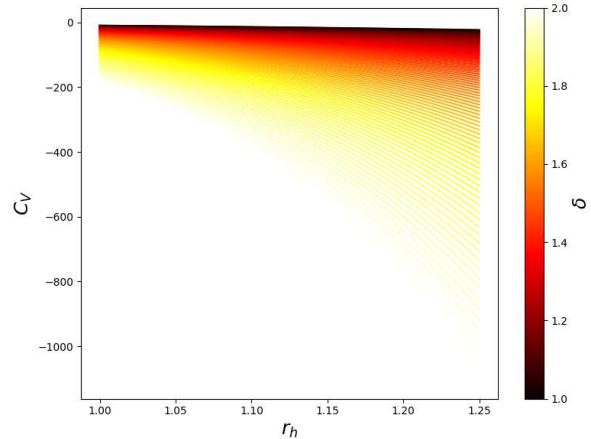
FIG. 5: Tsallis thermodynamic pressure P_T as a function of the horizon radius r_h for KR-ModMax black holes. The negative pressure indicates that, in this asymptotically flat setup, the effective cosmological contribution acts as a tension rather than a true pressure. Although both branches converge at large r_h where the mass term dominates, their distinct radial behavior at small r_h plays a crucial role in shaping the Joule-Thomson coefficient and the cooling-heating structure discussed in Sec. IV.

where a positive heat capacity corresponds to stability under thermal fluctuations, while a negative value signals local thermodynamic instability. Within the Tsallis framework adopted here, the heat capacity for the Kalb-Ramond-ModMax black hole can be evaluated analytically, yielding

$$C_V = -\frac{2\pi^{2\delta} [Mr_h(1-\ell)^2 e^\gamma - \zeta Q^2] r_h^{4\delta}}{2Mr_h(1-\ell)^2 e^\gamma - 3\zeta Q^2}. \quad (21)$$



(a) Ordinary ModMax branch ($\zeta = +1$). The heat capacity C_V remains negative throughout the explored range $r_h \in [1.0, 1.25]$, indicating local thermodynamic instability. As r_h increases, C_V approaches zero from below, signaling proximity to a Davies-type transition where the dominant instability weakens. The stratification with respect to the non-extensivity parameter δ reflects the increasing weight of entropy corrections near the transition region.



(b) Phantom ModMax branch ($\zeta = -1$). The heat capacity exhibits the same qualitative instability pattern but with systematically reduced magnitude. The absence of a zero-crossing confirms that no stable phase is realized, while the smoother approach toward $C_V \rightarrow 0^-$ indicates a weaker near-critical response compared to the ordinary branch.

FIG. 6: Heat capacity C_V as a function of the horizon radius r_h for KR-ModMax black holes within Tsallis non-extensive thermodynamics. Negative values throughout indicate local thermodynamic instability for both branches. The branch-dependent approach toward $C_V = 0^-$ at larger r_h plays a decisive role in shaping the Joule-Thomson cooling-heating behavior discussed in Sec. IV. The color scale corresponds to the non-extensivity parameter $\delta \in [1.0, 2.0]$.

The denominator of Eq. (21) vanishes at $r_h = 3\zeta Q^2 e^{-\gamma} / [2M(1-\ell)^2]$, indicating a divergence of C_V that separates thermodynamically distinct regimes.

The sign and magnitude of the heat capacity are strongly branch dependent. In the ordinary branch

$(\zeta = +1)$, the electromagnetic contribution counteracts the gravitational term, leading to negative heat capacity over a broad range of horizon radii. In the phantom branch $(\zeta = -1)$, the same contribution reinforces gravity, modifying the location and strength of the divergence but not altering the overall sign of C_V in the near-horizon region.

The behavior of the heat capacity is illustrated in Fig. 6 for representative parameter choices. In both branches, C_V remains negative over the displayed range of horizon radii, indicating local thermodynamic instability in the near-horizon regime. The ordinary branch (Fig. 6a) exhibits a monotonic increase of C_V toward zero as r_h grows, with the non-extensivity parameter δ producing a systematic stratification of the curves. The phantom branch (Fig. 6b) displays a similar qualitative trend, with slightly reduced magnitude, reflecting the reinforcing role of the electromagnetic sector.

The approach of C_V toward zero at larger horizon radii suggests proximity to a Davies-type transition [71], beyond which locally stable configurations may arise. However, within the parameter range explored here, both branches remain thermodynamically unstable at the local level, a feature that complements the global stability analysis based on the Helmholtz free energy and motivates the extended thermodynamic investigation presented in the next section.

IV. JOULE-THOMSON EXPANSION

The Joule-Thomson (JT) expansion provides a valuable diagnostic of thermodynamic response by examining the evolution of the Hawking temperature under isenthalpic processes. Within the extended thermodynamic framework developed above, it offers insight into how non-extensive effects and branch structure influence heating and cooling behavior beyond equilibrium considerations.

A. Joule-Thomson coefficient and inversion curve

The JT coefficient is defined as [72]

$$\mu_J = \left(\frac{\partial T_H}{\partial P_T} \right), \quad (22)$$

with $\mu_J > 0$ corresponding to cooling during expansion and $\mu_J < 0$ indicating heating. The inversion curve, defined by the condition $\mu_J = 0$, separates these regimes in the (P_T, T_H) plane [73].

For the Kalb-Ramond-ModMax black hole, explicit evaluation yields

$$\mu_J = \frac{4 \left[Mr_h (1 - \ell)^2 e^\gamma - \frac{3Q^2}{2} \right] \pi r_h^3}{\mathcal{B}}, \quad (23)$$

where

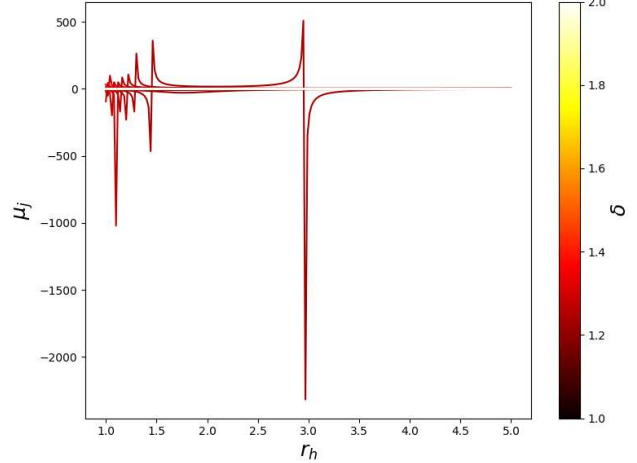


FIG. 7: Joule-Thomson (JT) coefficient μ_J as a function of the horizon radius r_h for the ordinary-branch KR-ModMax black hole ($M = 1, Q = 0.5, \zeta = +1, \gamma = 2, \ell = 0.5$). The color scale corresponds to the non-extensivity parameter $\delta \in [1.0, 2.0]$. Divergences of μ_J occur at $r_h \approx 1.2$ and $r_h \approx 2.7-3.0$, signaling inversion points that separate heating ($\mu_J < 0$) from cooling ($\mu_J > 0$) regimes during isenthalpic expansion. Increasing δ shifts the inversion radii toward larger r_h , demonstrating that non-extensive entropy systematically delays the onset of the cooling phase.

$$\mathcal{B} = 2M\pi^{2\delta} \left(\delta - \frac{5}{4} \right) (1 - \ell)^2 e^\gamma r_h^{4\delta+1} - 3\pi^{2\delta} \left(\delta - \frac{3}{2} \right) Q^2 r_h^{4\delta} - 5Mr_h(1 - \ell)^2 e^\gamma + 9Q^2. \quad (24)$$

The numerator of Eq. (23) vanishes at $r_h = 3Q^2 e^{-\gamma} / [2M(1 - \ell)^2]$, defining the inversion radius at which the JT coefficient changes sign. The location of this inversion point depends explicitly on the ModMax parameter γ , the KR deformation ℓ , and the non-extensivity parameter δ , highlighting the sensitivity of the JT process to the underlying microscopic structure.

B. Cooling-heating transitions and branch dependence

The behavior of the JT coefficient as a function of the horizon radius is illustrated in Fig. 7 for the ordinary branch. The coefficient exhibits pronounced divergences associated with the vanishing of the denominator \mathcal{B} , separating distinct thermodynamic response regimes. In the near-horizon region, μ_J is negative, indicating heating during expansion as electromagnetic contributions dominate. At intermediate radii, μ_J becomes positive, signaling a cooling regime in which the mass term governs the thermodynamic response. For sufficiently large horizon radii, the JT coefficient approaches small positive values and gradually stabilizes.

The non-extensivity parameter δ plays a crucial role in shaping the inversion structure. Increasing δ systematically shifts the inversion points toward larger horizon

radii, implying that non-extensive corrections delay the onset of the cooling regime by enhancing the entropy contribution in the inversion condition. This behavior reflects the fact that Tsallis entropy amplifies the weight of large-horizon configurations in the thermodynamic response.

Although the figure focuses on the ordinary branch, the analytic structure of Eq. (23) indicates that the branch parameter ζ influences both the location of divergences and the extent of cooling and heating regions. In particular, the reinforced electromagnetic contribution characterizing the phantom branch is expected to modify the balance between heating and cooling phases, in line with the enhanced thermal behavior observed in the previous sections. Overall, the JT expansion provides a sensitive probe of how non-extensive thermodynamics and branch structure jointly affect the response properties of Kalb-Ramond-ModMax black holes [58].

V. GRAVITATIONAL LENSING AND PHOTON SPHERES

Gravitational lensing provides a direct and geometry-driven probe of spacetime structure around compact objects, allowing deviations from general relativity to be tested without detailed assumptions about the nature of the light source [74, 75]. Since the first experimental confirmation of light deflection by the Sun, lensing has evolved into a precision tool for constraining modified gravity models, including scenarios with Lorentz symmetry breaking or nonlinear electromagnetic sectors [76]. In the weak-field regime, where the photon trajectory remains far from the event horizon, small deviations from the Schwarzschild prediction can accumulate into potentially observable signatures relevant to astrophysical lensing systems [77].

In the present context, weak gravitational lensing offers a sensitive diagnostic of the Kalb-Ramond-ModMax black hole. Although both the Kalb-Ramond condensate and the ModMax nonlinearity primarily affect the near-horizon geometry, their influence propagates to large distances through the optical structure of spacetime. To capture these effects in a coordinate-independent manner, we employ the Gauss-Bonnet (GB) theorem approach [42, 78, 79], which interprets the deflection of light as a global geometric effect governed by the integrated Gaussian curvature of an associated optical manifold.

A. Optical geometry and Gauss-Bonnet method

In static and spherically symmetric spacetimes, null geodesics can be equivalently described as spatial geodesics on an effective two-dimensional Riemannian manifold known as the optical geometry [80, 81]. Restricting the Kalb-Ramond-ModMax metric (1) to the equatorial plane ($\theta = \pi/2$), the corresponding optical

line element takes the form

$$ds^2 = \frac{dr^2}{f^2(r)} + \frac{r^2}{f(r)} d\phi^2, \quad (25)$$

where the lapse function $f(r)$ is given in Eq. (3). The conformal factor $1/f(r)$ encodes gravitational redshift effects and ensures that extremizing the optical path length reproduces the null geodesic equations via Fermat's principle [82].

The intrinsic curvature of the optical manifold is characterized by the Gaussian curvature K , which in two dimensions is fully determined by a single independent component of the Riemann tensor [83], namely

$$K = \frac{R_{r\phi r\phi}}{\det(g_{\text{opt}})}. \quad (26)$$

In the weak-field region ($r \gg r_h$), we expand the metric function asymptotically and retain terms up to $\mathcal{O}(r^{-5})$. This yields the following expression for the Gaussian curvature:

$$\begin{aligned} K \simeq & \frac{3\zeta Q^2}{r^4(1-\ell)^4 e^\gamma} - \frac{3\zeta Q^2 \ell}{r^4(1-\ell)^4 e^\gamma} + \frac{2M\ell^3}{r^3(1-\ell)^4} \\ & - \frac{6M\ell^2}{r^3(1-\ell)^4} + \frac{6M\ell}{r^3(1-\ell)^4} - \frac{2M}{r^3(1-\ell)^4} \\ & + \frac{3M^2\ell^4}{r^4(1-\ell)^4} - \frac{12M^2\ell^3}{r^4(1-\ell)^4} + \frac{18M^2\ell^2}{r^4(1-\ell)^4} \\ & - \frac{12M^2\ell}{r^4(1-\ell)^4} + \frac{3M^2}{r^4(1-\ell)^4}. \end{aligned} \quad (27)$$

The leading r^{-3} contributions originate from the mass sector, while the r^{-4} terms encode both second-order mass corrections and the charge-dependent ModMax contributions, controlled by the branch parameter ζ and the suppression factor $e^{-\gamma}$. The Kalb-Ramond parameter ℓ enters universally through the prefactor $(1-\ell)^{-4}$, amplifying all curvature contributions as ℓ approaches unity.

The Gauss-Bonnet theorem provides a direct link between this intrinsic curvature and the total deflection angle experienced by a light ray. Applied to a non-singular domain \mathcal{D}_∞ exterior to the photon trajectory, the theorem yields the coordinate-independent expression [42]

$$\beta = - \iint_{\mathcal{D}_\infty} K dS, \quad (28)$$

where dS denotes the surface element of the optical manifold. In the weak-lensing approximation, the photon path is well approximated by the unperturbed straight-line trajectory $r = b/\sin \phi$, allowing the integral to be evaluated analytically. The resulting deflection angle, together with its branch-dependent structure and limiting behavior, is discussed in the following subsection.

B. Weak-field deflection angle and branch-dependent signatures

Within the Gauss-Bonnet framework, the total deflection angle experienced by a light ray with impact parameter b is determined by the surface integral of the Gaussian curvature over the exterior optical domain \mathcal{D}_∞ , namely

$$\beta = - \iint_{\mathcal{D}_\infty} K dS, \quad (29)$$

where the integration region is bounded by the photon trajectory and an asymptotic reference curve [42]. In the weak-field regime, the photon path is well approximated by the unperturbed straight-line trajectory $r = b/\sin \phi$, which allows the integral to be evaluated analytically.

Carrying out the integration using the asymptotic expansion of the Gaussian curvature given in Eq. (27), we obtain the vacuum deflection angle for the Kalb-Ramond-ModMax black hole,

$$\begin{aligned} \beta_{\text{vac}} \approx & \frac{4M}{b(1-\ell)^4} - \frac{12M\ell}{b(1-\ell)^4} + \frac{12M\ell^2}{b(1-\ell)^4} - \frac{4M\ell^3}{b(1-\ell)^4} \\ & + \frac{15\pi M^2}{4b^2(1-\ell)^4} - \frac{3\pi M^2\ell}{2b^2(1-\ell)^4} + \frac{3\pi M^2\ell^3}{2b^2(1-\ell)^4} - \frac{3\pi M^2\ell^4}{4b^2(1-\ell)^4} \\ & - \frac{3\pi Q^2\zeta}{4b^2(1-\ell)^4 e^\gamma} + \frac{3\pi Q^2\zeta\ell}{4b^2(1-\ell)^4 e^\gamma} - \frac{4MQ^2\zeta}{3b^3(1-\ell)^4 e^\gamma} \\ & + \frac{8MQ^2\ell^2\zeta}{3b^3(1-\ell)^4 e^\gamma} - \frac{4MQ^2\ell\zeta}{3b^3(1-\ell)^4 e^\gamma} + \mathcal{O}(M^3, 1/b^4). \end{aligned} \quad (30)$$

This expression naturally decomposes into three classes of contributions: (i) mass terms proportional to M/b and M^2/b^2 , (ii) Kalb-Ramond corrections controlled by powers of ℓ and the universal amplification factor $(1-\ell)^{-4}$, and (iii) charge-dependent ModMax terms proportional to $Q^2\zeta$, whose magnitude is suppressed by $e^{-\gamma}$ and whose sign is fixed by the branch parameter ζ .

Several physically relevant limits follow immediately. In the Schwarzschild limit ($\ell \rightarrow 0, \gamma \rightarrow 0, Q \rightarrow 0$), Eq. (30) reduces to

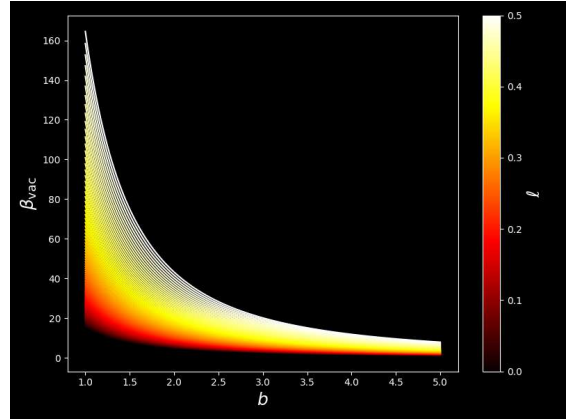
$$\beta_{\text{Sch}} = \frac{4M}{b} + \frac{15\pi M^2}{4b^2} + \mathcal{O}(b^{-3}), \quad (31)$$

recovering the standard general-relativistic result [84, 85]. For the ordinary branch ($\zeta = +1$) with $\ell \rightarrow 0$ and $\gamma \rightarrow 0$, the expression reduces to the Reissner-Nordström deflection angle, i.e.

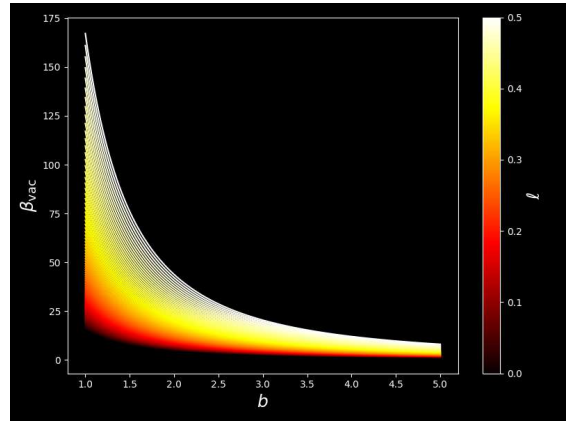
$$\beta_{\text{RN}} = \frac{4M}{b} + \frac{15\pi M^2}{4b^2} - \frac{3\pi Q^2}{4b^2} - \frac{4MQ^2}{3b^3} + \mathcal{O}(b^{-4}), \quad (32)$$

where the electromagnetic contribution partially counteracts gravitational focusing.

On the other hand, in the phantom branch ($\zeta = -1$) the sign reversal of the charge sector transforms the electromagnetic contribution into an additional focusing mechanism. Even in the limit $\ell \rightarrow 0$ and $\gamma \rightarrow 0$, the deflection



(a) Ordinary branch ($\zeta = +1$).



(b) Phantom branch ($\zeta = -1$).

FIG. 8: Vacuum deflection angle β_{vac} as a function of the impact parameter b for KR-ModMax black holes with fixed $M = 1, Q = 0.5$, and $\gamma = 2$. The color scale indicates the Kalb-Ramond parameter $\ell \in [0, 0.5]$. Panel (a) shows the ordinary branch ($\zeta = +1$), where the electromagnetic contribution partially counteracts gravitational focusing, leading to suppressed deflection at small b . Increasing ℓ enhances the mass-dominated terms through the $(1-\ell)^{-4}$ amplification. Panel (b) displays the phantom branch ($\zeta = -1$), where the sign reversal of the electromagnetic sector transforms the charge contribution into an additional focusing mechanism. Consequently, the deflection angle remains strictly positive and is notably enhanced at small b , exceeding the ordinary-branch values by up to an order of magnitude as ℓ increases. This qualitative distinction serves as an observational discriminator between the two electromagnetic sectors.

angle becomes

$$\beta_{\text{phantom}} = \frac{4M}{b} + \frac{15\pi M^2}{4b^2} + \frac{3\pi Q^2}{4b^2} + \frac{4MQ^2}{3b^3} + \mathcal{O}(b^{-4}), \quad (33)$$

which has no analogue in standard general relativity. In this sector, both mass and charge contribute constructively to light bending, leading to systematically larger deflection angles.

These qualitative differences are evident in the numerical results shown in Fig. 8, where the deflection angle is plotted for varying Kalb-Ramond parameter $\ell \in [0, 0.5]$ at fixed $\gamma = 2$. In the ordinary branch, the competition between mass-induced focusing and charge-induced defocusing produces smaller deflection angles, particularly at low ℓ . As ℓ increases, the universal amplification factor $(1 - \ell)^{-4}$ enhances all contributions, leading to progressively larger deflection at all impact parameters. In the phantom branch, the deflection angle remains strictly positive and is substantially enhanced relative to the ordinary branch, exceeding the latter by more than an order of magnitude at small b for larger ℓ values. This pronounced enhancement provides a clear geometric manifestation of the branch dichotomy.

From an observational perspective, these branch-dependent signatures translate into potentially measurable effects. Phantom configurations would produce significantly larger Einstein ring radii and enhanced magnification in strong-lensing systems, while the ℓ -dependence of the weak-field deflection could imprint small but systematic astrometric shifts in high-precision measurements of stellar orbits near supermassive black holes. Together with the thermodynamic and photonsphere properties discussed in previous sections, gravitational lensing offers a complementary channel for discriminating between the ordinary and phantom Kalb-Ramond-ModMax black hole branches.

VI. PLASMA EFFECTS ON PHOTON PROPAGATION

In realistic astrophysical environments, black holes are rarely isolated systems. Instead, they are typically surrounded by plasma-rich media such as accretion disks, stellar winds, or diffuse interstellar matter, all of which modify photon propagation through dispersive effects [86]. In contrast to vacuum null geodesics, light rays propagating in plasma experience frequency-dependent refraction, leading to shifts in photon trajectories, photonsphere locations, and shadow properties.

For the Kalb-Ramond-ModMax black hole, incorporating plasma effects is therefore essential for bridging the gap between theoretical predictions and observational applications, particularly in the context of horizon-scale imaging and lensing measurements by instruments such as the Event Horizon Telescope [87]. In this section, we analyze photon dynamics in a dispersive plasma medium and derive the modified conditions for circular photon orbits that define the photon sphere.

A. Photon dynamics and photon spheres in plasma

Photon propagation in a plasma medium can be described using an effective Hamiltonian formalism that incorporates the dispersive response of the medium [88].

For a static plasma distribution in the Kalb-Ramond-ModMax spacetime, the Hamiltonian governing photon motion takes the form

$$H = \frac{1}{2} [g^{\alpha\beta} p_\alpha p_\beta + (\omega_p^2 - 1)(p_\alpha u^\alpha)^2], \quad (34)$$

where p_α denotes the photon four-momentum, u^α is the plasma four-velocity, and ω_p is the local plasma frequency. Assuming a static plasma configuration, the four-velocity is given by $u^\alpha = f^{-1/2} \delta_t^\alpha$, where $f(r)$ is the KR-ModMax lapse function defined in Eq. (3).

The dispersive nature of the plasma is encoded in the refractive index,

$$n^2 = 1 - \frac{\omega_p^2}{\omega^2}, \quad (35)$$

where ω denotes the photon frequency measured by a local static observer. The plasma frequency itself is determined by the electron number density $N(r)$ through

$$\omega_p^2(r) = \frac{4\pi e^2 N(r)}{m_e}, \quad (36)$$

with e and m_e representing the electron charge and mass, respectively. A photon detected at spatial infinity with frequency ω_0 undergoes gravitational redshift as it propagates inward, such that

$$\omega(r) = \frac{\omega_0}{\sqrt{f(r)}}. \quad (37)$$

The vacuum limit is recovered smoothly by setting $\omega_p \rightarrow 0$, in which case the Hamiltonian reduces to the standard null geodesic condition $g^{\alpha\beta} p_\alpha p_\beta = 0$.

Restricting attention to the equatorial plane ($\theta = \pi/2$), Hamilton's equations yield the equations of motion

$$\dot{t} = -\frac{p_t}{f(r)}, \quad \dot{r} = f(r)p_r, \quad \dot{\varphi} = \frac{p_\varphi}{r^2}, \quad (38)$$

where the overdot denotes differentiation with respect to an affine parameter. Imposing the Hamiltonian constraint leads to the radial orbit equation

$$\frac{dr}{d\varphi} = r \sqrt{f(r)} \sqrt{h^2(r) \frac{\omega_0^2}{p_\varphi^2} - 1}, \quad (39)$$

where the optical impact function $h(r)$ is defined as [25]

$$h^2(r) = r^2 \left(\frac{1}{f(r)} - \frac{\omega_p^2(r)}{\omega_0^2} \right). \quad (40)$$

Unstable circular photon orbits, which determine the photon sphere and the boundary of the black hole shadow, correspond to extrema of the impact function $h^2(r)$. The photon-sphere radius r_p is therefore obtained from the condition

$$\frac{d}{dr} \left[r^2 \left(\frac{1}{f(r)} - \frac{\omega_p^2(r)}{\omega_0^2} \right) \right]_{r=r_p} = 0, \quad (41)$$

or equivalently,

$$\frac{2}{f(r_p)} - \frac{2\omega_p^2(r_p)}{\omega_0^2} - r_p \left(\frac{f'(r_p)}{f^2(r_p)} + \frac{2\omega_p(r_p)\omega'_p(r_p)}{\omega_0^2} \right) = 0. \quad (42)$$

This condition generalizes the standard vacuum photon-sphere equation by incorporating plasma effects through both the local plasma frequency $\omega_p(r_p)$ and its radial gradient $\omega'_p(r_p)$. As a result, the photon-sphere radius becomes explicitly frequency dependent and sensitive to the plasma distribution, providing a direct channel through which environmental effects can modify observable shadow and lensing properties.

B. Homogeneous versus inhomogeneous plasma distributions

The influence of plasma on photon-sphere properties depends crucially on the spatial structure of the medium. To disentangle intrinsic spacetime effects from environmental contributions, we examine two representative scenarios: a homogeneous plasma with constant plasma frequency and an inhomogeneous plasma with a radially stratified density profile.

For a spatially uniform plasma, the plasma frequency is constant, $\omega_p = \text{const.}$, and the gradient term in Eq. (42) vanishes. The photon-sphere condition then reduces to

$$\frac{2}{f(r_p)} - \frac{2\omega_p^2}{\omega_0^2} = r_p \frac{f'(r_p)}{f^2(r_p)}, \quad (43)$$

which can be solved numerically for the Kalb-Ramond-ModMax metric function (3) at fixed values of the plasma-to-photon frequency ratio ω_p^2/ω_0^2 .

The results summarized in Table II reveal several robust trends. First, the presence of plasma systematically shifts the photon sphere outward for both branches. As the ratio ω_p^2/ω_0^2 increases, the effective propagation speed of photons decreases, weakening curvature-induced focusing and pushing unstable circular orbits to larger radii. Quantitatively, increasing ω_p^2/ω_0^2 from 0 to 0.20 leads to a shift $\Delta r_p \approx 0.07$ for the ordinary branch and $\Delta r_p \approx 0.09$ for the phantom branch.

Second, the branch dichotomy remains clearly visible in homogeneous plasma. For identical values of (ℓ, γ) , the phantom branch ($\zeta = -1$) consistently produces larger photon-sphere radii than the ordinary branch ($\zeta = +1$). In vacuum and at $\gamma = 0$, this difference reaches $\Delta r_p \approx 0.53$, corresponding to an enhancement of roughly 25%. Importantly, this separation persists across all plasma densities, indicating that it originates from the intrinsic sign reversal of the electromagnetic sector rather than from plasma effects.

Finally, the ModMax parameter γ affects the two branches in qualitatively different ways. In the ordinary branch, increasing γ suppresses the effective charge contribution through the factor $e^{-\gamma}$ and shifts the geometry toward the Schwarzschild-Kalb-Ramond limit,

TABLE II: Photon sphere radius r_p for KR-ModMax black holes in homogeneous plasma with fixed $M = 1$, $\ell = 0.2$, and $Q = 0.5$. The ordinary branch ($\zeta = +1$) yields smaller photon sphere radii due to the repulsive electromagnetic contribution, while the phantom branch ($\zeta = -1$) produces larger r_p from enhanced gravitational focusing. Increasing plasma density (ω_p^2/ω_0^2) uniformly shifts r_p outward for both branches.

ζ	γ	ω_p^2/ω_0^2	r_p
Ordinary Branch ($\zeta = +1$)			
+1	0	0.00	2.103
+1	0	0.05	2.118
+1	0	0.10	2.134
+1	0	0.20	2.171
+1	1	0.00	2.300
+1	1	0.05	2.317
+1	1	0.10	2.334
+1	1	0.20	2.374
Phantom Branch ($\zeta = -1$)			
-1	0	0.00	2.637
-1	0	0.05	2.656
-1	0	0.10	2.677
-1	0	0.20	2.723
-1	1	0.00	2.492
-1	1	0.05	2.510
-1	1	0.10	2.530
-1	1	0.20	2.573

resulting in a moderate increase of r_p . In the phantom branch, the same increase in γ partially suppresses the enhanced focusing induced by the phantom charge, leading instead to a decrease of the photon-sphere radius. This opposite response provides an additional handle for distinguishing between the two branches in weakly stratified environments.

Now, astrophysical plasmas are typically radially stratified rather than homogeneous. To model this situation, we consider a power-law plasma profile,

$$\omega_p^2(r) = \frac{\kappa_0}{r^\alpha}, \quad (44)$$

with $\alpha = 1$, which captures the characteristic $1/r$ falloff expected in stellar winds and accretion flows. Substituting this profile into Eq. (42) yields

$$\frac{2}{f(r_p)} - \frac{2\kappa_0}{r_p \omega_0^2} - r_p \left(\frac{f'(r_p)}{f^2(r_p)} + \frac{2\kappa_0^2}{r_p^3 \omega_0^2} \right) = 0, \quad (45)$$

which must again be solved numerically.

The results collected in Table III display a markedly different hierarchy of effects. In this case, the photon-sphere radius is dominated by the Kalb-Ramond parameter ℓ ,

TABLE III: Photon sphere radius r_p for KR-ModMax black holes in inhomogeneous plasma ($\alpha = 1$) with fixed $M = 1$, $Q = 0.5$, $\kappa_0 = 1$, and $\omega_0 = 0.5$. The KR parameter ℓ dominates the photon sphere structure, producing a four-fold increase in r_p as ℓ increases from 0.1 to 0.8. The ModMax branch parameter ζ and nonlinearity γ produce only marginal corrections at the third decimal place.

ℓ	ζ	γ	r_p
Weak KR Deformation ($\ell = 0.1$)			
0.1	+1	0	4.734
0.1	+1	1	4.773
0.1	-1	0	4.860
0.1	-1	1	4.819
Moderate KR Deformation ($\ell = 0.5$)			
0.5	+1	0	8.447
0.5	+1	1	8.452
0.5	-1	0	8.465
0.5	-1	1	8.459
Strong KR Deformation ($\ell = 0.8$)			
0.8	+1	0	20.762
0.8	+1	1	20.763
0.8	-1	0	20.765
0.8	-1	1	20.764

with only marginal sensitivity to the ModMax sector. As ℓ increases from 0.1 to 0.8, the photon-sphere radius grows by more than a factor of four, reflecting the strong amplification induced by the asymptotic rescaling $(1 - \ell)^{-1}$ in combination with the radially varying refractive index.

On the other hand, variations in the branch parameter ζ and in the ModMax parameter γ produce only minute shifts in r_p , typically at the level $\Delta r_p \sim 10^{-3}\text{-}10^{-2}$. For instance, at $\ell = 0.8$ the difference between the ordinary and phantom branches is reduced to $\Delta r_p \approx 0.003$, compared to $\Delta r_p \approx 0.53$ in the homogeneous case. This strong suppression indicates that the plasma gradient dominates the effective optical potential, effectively masking the sign-sensitive electromagnetic contributions.

We close this subsection by discussing the physical and observational implications. The contrast between homogeneous and inhomogeneous plasma regimes has direct implications for black-hole imaging. In homogeneous or weakly stratified media, the photon-sphere radius retains clear sensitivity to the electromagnetic branch structure, and the sizable separation between ordinary and phantom configurations could, in principle, be probed through precise measurements of shadow sizes or frequency-dependent lensing. In strongly stratified environments, however, plasma effects and Kalb-Ramond-induced rescaling dominate photon dynamics,

rendering branch discrimination observationally challenging.

At the same time, the pronounced sensitivity of the photon-sphere radius to the Lorentz-symmetry-breaking parameter ℓ in inhomogeneous plasma suggests that high-resolution, multi-frequency observations could place meaningful constraints on such deformations, provided that plasma properties are modeled accurately. Overall, these results reveal the necessity of incorporating realistic plasma distributions when attempting to extract fundamental gravitational or electromagnetic physics from horizon-scale observations.

VII. TIDAL FORCES AND BRANCH-DEPENDENT DEFORMATIONS

Tidal effects acting on extended bodies provide a direct probe of spacetime curvature beyond the idealized motion of pointlike test particles. While geodesic trajectories encode the global structure of a gravitational field, finite-sized objects respond to local curvature gradients through differential accelerations governed by the Riemann tensor. In strong-field regimes, these tidal deformations can exhibit qualitative features that are invisible at the level of geodesic motion alone.

In the Kalb-Ramond-ModMax framework, the combined presence of Lorentz-symmetry-breaking effects and nonlinear electrodynamics modifies the radial dependence of the metric function relative to standard electrovacuum solutions. As a result, the tidal response of infalling matter can depart significantly from the familiar Schwarzschild or Reissner-Nordström behavior. In this section, we analyze tidal forces in the ordinary and phantom branches and identify branch-dependent deformation patterns with no counterpart in general relativity.

A. Geodesic deviation and tidal forces

The relative acceleration between neighboring freely falling worldlines is governed by the geodesic deviation equation [89]

$$\frac{D^2\eta^\mu}{D\tau^2} = -R^\mu_{\nu\alpha\beta} u^\nu u^\alpha \eta^\beta, \quad (46)$$

where η^μ denotes the separation vector between nearby geodesics, u^μ is the four-velocity of the reference worldline, and τ is the proper time. The Riemann curvature tensor acts as the mediator of tidal interactions, converting spacetime geometry into physically measurable distortions of extended bodies.

To obtain physically transparent tidal forces, it is convenient to project the curvature tensor onto an orthonormal tetrad adapted to static observers. Introducing the basis [90, 91]

$$e_0 = f^{-1/2} \partial_t,$$

$$\begin{aligned} e_{\hat{1}} &= f^{1/2} \partial_r, \\ e_{\hat{2}} &= \frac{1}{r} \partial_\theta, \\ e_{\hat{3}} &= \frac{1}{r \sin \theta} \partial_\varphi, \end{aligned} \quad (47)$$

the metric locally reduces to the Minkowski form $\eta_{\hat{a}\hat{b}} = \text{diag}(-1, 1, 1, 1)$.

In this frame, tidal forces are encoded in the electric part of the Riemann tensor,

$$\mathcal{E}_{\hat{i}\hat{j}} = R_{\hat{0}\hat{i}\hat{0}\hat{j}}, \quad (48)$$

which directly determines the relative acceleration of nearby freely falling particles. For any static, spherically symmetric spacetime, the independent nonvanishing components reduce to

$$\mathcal{E}_{\hat{1}\hat{1}} = -\frac{1}{2} f''(r), \quad \mathcal{E}_{\hat{2}\hat{2}} = \mathcal{E}_{\hat{3}\hat{3}} = -\frac{f'(r)}{2r}, \quad (49)$$

with spherical symmetry enforcing equality of the two angular components.

For the Kalb-Ramond-ModMax black hole, the first and second radial derivatives of the metric function (3) are given by

$$f'(r) = \frac{2M}{r^2} - \frac{2\zeta Q^2 e^{-\gamma}}{(1-\ell)^2 r^3}, \quad (50)$$

$$f''(r) = -\frac{4M}{r^3} + \frac{6\zeta Q^2 e^{-\gamma}}{(1-\ell)^2 r^4}. \quad (51)$$

Substituting these expressions into the geodesic deviation equation yields the explicit tidal accelerations,

$$\frac{D^2 \eta_{\hat{1}}}{D\tau^2} = \left(\frac{2M}{r^3} - \frac{3\zeta Q^2 e^{-\gamma}}{(1-\ell)^2 r^4} \right) \eta_{\hat{1}}, \quad (52)$$

$$\frac{D^2 \eta_{\hat{i}}}{D\tau^2} = \left(-\frac{M}{r^3} + \frac{\zeta Q^2 e^{-\gamma}}{(1-\ell)^2 r^4} \right) \eta_{\hat{i}}, \quad \hat{i} = \hat{2}, \hat{3}. \quad (53)$$

At large radii, the leading r^{-3} terms dominate, recovering the familiar Schwarzschild tidal pattern characterized by radial stretching accompanied by angular compression. Closer to the black hole, however, the charge-dependent terms scale more steeply with radius and can significantly reshape the tidal profile. The manner in which these corrections compete or reinforce the Schwarzschild contribution depends crucially on the electromagnetic branch parameter ζ , setting the stage for qualitatively distinct tidal behaviors in the ordinary and phantom sectors.

B. Tidal inversion and physical implications

A distinctive feature of the Kalb-Ramond-ModMax black hole is the possibility of tidal-force inversion, namely the vanishing and subsequent sign reversal of

tidal accelerations at finite radii outside the event horizon. This phenomenon has no analogue in the Schwarzschild spacetime and arises from the competition between the mass-induced curvature and the charge-dependent contributions controlled by the Kalb-Ramond and ModMax sectors.

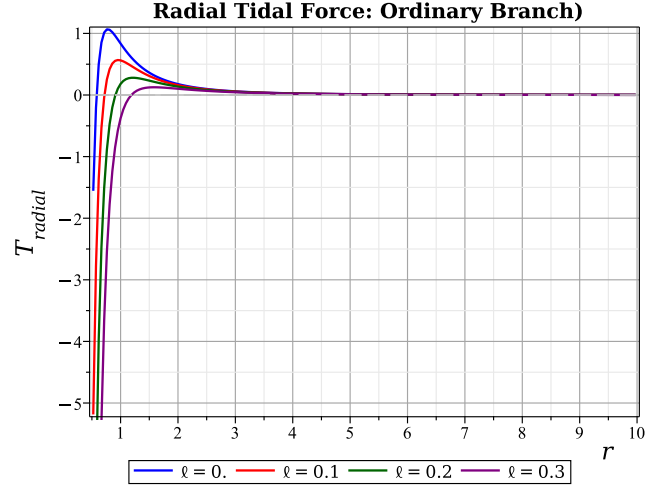


FIG. 9: Radial tidal acceleration T_{rad} as a function of r for different values of the Lorentz-violating parameter ℓ in the ordinary branch ($\zeta = +1$). Increasing ℓ shifts the zero-crossing radius R_{rad} to larger values and enhances the tidal forces at intermediate radii. Parameters: $M = 1$, $Q = 0.8$, $\gamma = 0.5$.

The sensitivity of tidal forces to the Lorentz-symmetry-breaking parameter ℓ is illustrated in Fig. 9 for the ordinary branch. As ℓ increases, the factor $(1-\ell)^{-2}$ amplifies the charge-dependent terms in Eqs. (52)-(53) relative to the Schwarzschild contribution. This produces two correlated effects: the magnitude of the tidal acceleration at fixed intermediate radii increases, and the radial location at which the radial tidal force vanishes is shifted outward. Physically, stronger Lorentz violation enlarges the region where charge-induced corrections dominate the tidal response, thereby extending the domain of tidal inversion.

The characteristic transition scales are quantified by the tidal balance radii R_{rad} and R_{ang} , defined by the vanishing of the radial and angular tidal components, respectively. Their dependence on the electric charge and model parameters is displayed in Fig. 10 and summarized numerically in Table IV. The data reveal systematic trends: both balance radii increase with ℓ due to the universal $(1-\ell)^{-2}$ enhancement, while increasing the ModMax parameter γ suppresses the charge contribution through the factor $e^{-\gamma}$, shifting the inversion radii inward. For representative parameter choices, the balance radii span the range $R_{\text{rad}}, R_{\text{ang}} \sim 0.1\text{-}2$ in units of the black-hole mass, indicating that tidal inversion may occur either close to the horizon or well outside it, depending on the regime.

The existence and physical relevance of these inversion

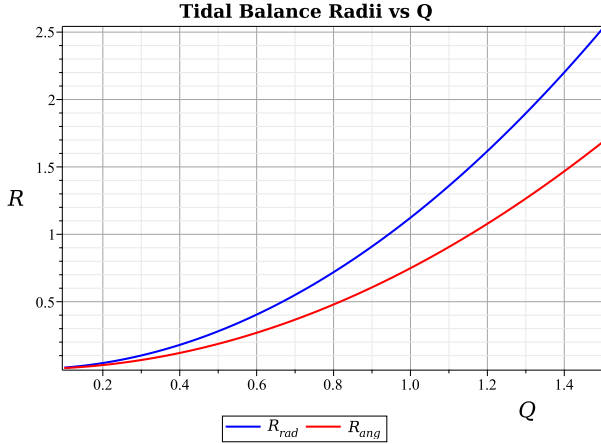


FIG. 10: Tidal balance radii R_{rad} (blue) and R_{ang} (red) as functions of the electric charge Q for the ordinary ModMax branch ($\zeta = +1$). Both radii scale quadratically with Q and preserve the universal ratio $R_{\text{rad}}/R_{\text{ang}} = 3/2$, independent of model parameters. Parameters: $M = 1$, $\ell = 0.1$, $\gamma = 0.5$.

TABLE IV: Tidal balance radii for the KR-ModMax BH in the ordinary branch ($\zeta = +1$), with $M = 1$ and $Q = 0.8$. The ratio $R_{\text{rad}}/R_{\text{ang}} = 3/2$ holds universally.

ℓ	γ	R_{rad}	R_{ang}
0.00	0.0	0.9600	0.6400
0.00	0.5	0.5823	0.3882
0.00	1.0	0.3532	0.2354
0.00	1.5	0.2142	0.1428
0.10	0.0	1.1852	0.7901
0.10	0.5	0.7189	0.4792
0.10	1.0	0.4360	0.2907
0.10	1.5	0.2645	0.1763
0.20	0.0	1.5000	1.0000
0.20	0.5	0.9098	0.6065
0.20	1.0	0.5518	0.3679
0.20	1.5	0.3347	0.2231
0.30	0.0	1.9592	1.3061
0.30	0.5	1.1883	0.7922
0.30	1.0	0.7207	0.4805
0.30	1.5	0.4372	0.2914

scales depend crucially on the electromagnetic branch parameter ζ . For the ordinary ModMax branch ($\zeta = +1$), the charge contribution enters the tidal tensor with a sign opposite to the Schwarzschild term at sufficiently small radii. As shown in Fig. 11, radial tidal stretching weakens as the black hole is approached, vanishes at R_{rad} , and is subsequently replaced by radial compression. Simultaneously, angular compression is softened and reverses at R_{ang} . This regulated tidal environment represents a

qualitative departure from the classical spaghettiification scenario and suggests that the Kalb-Ramond-ModMax corrections act as an effective curvature-softening mechanism. Such behavior could influence the coherence, deformation, and survivability of extended structures such as accretion streams or plasma filaments in the strong-field region.

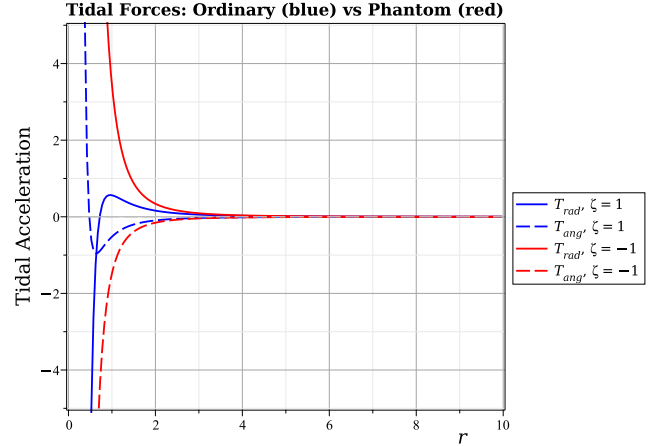


FIG. 11: Radial (solid lines) and angular (dashed lines) tidal acceleration components for KR-ModMax black holes, evaluated in an orthonormal frame. Blue curves correspond to the ordinary branch ($\zeta = +1$), while red curves represent the phantom branch ($\zeta = -1$). The horizontal gray dashed line marks vanishing tidal acceleration. For the ordinary branch, both components cross zero at finite radii, whereas no zero crossing occurs for the phantom branch. Parameters: $M = 1$, $Q = 0.8$, $\ell = 0.1$, $\gamma = 0.5$.

On the other hand, for the phantom branch ($\zeta = -1$) the electromagnetic contribution reinforces the Schwarzschild tidal field rather than opposing it. In this case, both R_{rad} and R_{ang} become negative and therefore lose any direct geometric meaning. Radial stretching and angular compression persist throughout the exterior region and grow monotonically toward the horizon, producing tidal stresses that are even stronger than those encountered in standard general relativity. This behavior reflects the exotic energy content of the phantom ModMax sector and indicates a dynamically harsher environment for infalling extended matter.

The aforementioned dichotomy between the two branches reveals the sensitivity of tidal observables to the underlying nonlinear electrodynamic structure. While both branches are mathematically admissible solutions of the Einstein-Kalb-Ramond-ModMax equations, tidal dynamics provide a physically transparent discriminator between them. When combined with thermodynamic behavior and optical signatures such as gravitational lensing and photon-sphere properties, tidal effects furnish an independent and complementary probe for assessing the physical viability of ordinary versus phantom regimes in this class of Lorentz-violating black-hole models.

From a physical standpoint, the existence or absence

of tidal inversion constitutes an independent diagnostic of branch viability. In the ordinary ModMax branch, the partial cancellation between the Schwarzschild and electromagnetic contributions leads to a regulated strong-field tidal environment, in which extreme spaghettification is softened within a finite radial interval outside the horizon. By contrast, the phantom branch exhibits no such regulation: tidal stretching and angular compression are uniformly enhanced, producing a dynamically harsher environment for extended matter.

Importantly, this distinction is entirely local and does not rely on thermodynamic equilibrium or asymptotic optical measurements. When combined with the thermodynamic phase structure and the branch-dependent lensing and photon-sphere properties discussed in previous sections, tidal forces therefore provide a complementary and physically transparent probe of the underlying nonlinear electrodynamic sector.

VIII. CONCLUSIONS

In this work we have explored a charged black-hole solution arising from the simultaneous presence of a Kalb-Ramond (KR) three-form condensate and ModMax nonlinear electrodynamics, focusing on the physical implications of the resulting branch structure. The motivation behind this study was twofold. On one hand, both ingredients are well motivated independently: the Kalb-Ramond field naturally appears in string-inspired effective theories and induces controlled Lorentz-symmetry-breaking effects, while ModMax electrodynamics represents the unique conformal and duality-invariant deformation of Maxwell theory. On the other hand, their combined impact on black-hole physics has remained largely unexplored, despite the fact that each sector modifies gravity in a distinct and potentially observable way. Our aim was therefore to assess whether their interplay leads merely to quantitative corrections, or instead to qualitatively new physical behavior.

The resulting KR-ModMax black hole is governed, beyond mass and charge, by three deformation parameters: the Lorentz-symmetry-breaking parameter ℓ , the ModMax nonlinearity parameter γ , and the discrete branch selector $\zeta = \pm 1$. A central outcome of our analysis is that the branch parameter ζ acts as a genuine physical discriminator. Already at the level of the spacetime geometry, the ordinary branch ($\zeta = +1$) admits the familiar hierarchy of non-extremal, extremal, and naked configurations, while the phantom branch ($\zeta = -1$) generically supports a single-horizon structure. This geometric distinction propagates coherently through all physical sectors that we investigated, providing a unifying theme for the entire analysis.

We examined the thermodynamic properties of the KR-ModMax black hole within the non-extensive Tsallis entropy framework, which is particularly suited to gravitational systems characterized by long-range correlations.

The Hawking temperature exhibits branch-dependent behavior: charge effects suppress the temperature in the ordinary branch, allowing for extremal configurations, whereas in the phantom branch the temperature is uniformly enhanced and never vanishes. The Tsallis deformation parameter δ reshapes the thermodynamic landscape, modifying the internal energy, Helmholtz free energy, and effective pressure. The heat capacity proved especially informative: while the ordinary branch can approach regimes suggestive of thermodynamic stabilization, the phantom branch remains dominated by negative heat capacity, indicating persistent local instability. These features are further reinforced by the Joule-Thomson expansion, where well-defined inversion curves appear primarily in the ordinary branch, whereas the phantom sector exhibits a more restricted and less structured cooling-heating behavior.

Optical properties provide an independent and complementary window into the branch structure. Using the Gauss-Bonnet approach to weak gravitational lensing, we found that the ordinary branch generally produces reduced deflection angles compared to the Schwarzschild case, reflecting the partially repulsive role of the electromagnetic sector. In contrast, the phantom branch yields systematically enhanced deflection, since the sign-reversed electromagnetic contribution reinforces gravitational focusing. This distinction persists, in a modified form, when photon propagation is studied in plasma environments. In homogeneous plasma, branch-dependent shifts of the photon-sphere radius remain visible, while in strongly stratified plasma distributions the optical structure becomes dominated by the Lorentz-symmetry-breaking parameter ℓ , with ModMax effects largely suppressed. This hierarchy reveals the importance of accurate plasma modeling when attempting to extract fundamental physics from black-hole shadow observations.

Tidal forces offer a direct probe of the local curvature structure that is independent of both thermodynamic equilibrium and asymptotic optical measurements. By analyzing geodesic deviation in an orthonormal frame, we identified two characteristic tidal balance radii at which radial and angular tidal components vanish. For the ordinary branch, these radii are positive and physically meaningful, signaling a partial inversion of the classical spaghettification pattern: radial stretching and angular compression are softened and can reverse inside a finite region outside the horizon. Remarkably, the ratio of these radii is universal and independent of all model parameters. The phantom branch, by contrast, admits no such tidal inversion; tidal forces are uniformly intensified as the horizon is approached. This sharp dichotomy provides a physically transparent criterion for assessing branch viability and reinforces the conclusions drawn from thermodynamic and optical analyses.

Taken together, our results demonstrate that the KR-ModMax black hole is not merely a perturbative deformation of Reissner-Nordström geometry, but a theoretically motivated system with a rich and internally consistent

physical structure. The ordinary branch retains continuity with standard charged black holes while introducing controlled, potentially observable deviations. The phantom branch, although mathematically admissible, displays a combination of enhanced lensing, stronger tidal forces, and persistent thermodynamic instability that may challenge its physical realizability, or alternatively render it particularly easy to distinguish observationally.

Extending the analysis to rotating configurations would greatly enhance the astrophysical relevance of the model. Moreover, quasinormal modes and gravitational-wave ringdown signatures could provide additional observational discriminants. Additionally, a systematic comparison between Tsallis entropy and other generalized entropy formalisms may further illuminate the role of non-extensivity in black-hole thermodynamics. Finally, embedding the KR-ModMax framework within a more fundamental string-theoretic or supergravity setting could clarify the microscopic origin and allowed ranges of the parameters ℓ , γ , and ζ . All these studies will be performed in future projects.

In conclusion, the combined presence of Kalb-Ramond Lorentz-symmetry breaking and ModMax nonlinear electrodynamics leads to a black-hole phenomenology that is both rich and sharply structured. The branch parameter ζ emerges as the key organizing principle, controlling geometry, thermodynamics, optics, and tidal dynamics in a unified way, and offering multiple, complementary pathways for confronting this class of models with observations.

ACKNOWLEDGMENTS

I. S. and E. S. thank TÜBİTAK, ANKOS, and SCOAP3 for academic support. The authors acknowledge the contribution of the LISA Cosmology Working Group (CosWG), as well as support from the COST Actions CA21136 - Addressing observational tensions in cosmology with systematics and fundamental physics (CosmoVerse) - CA23130, Bridging high and low energies in search of quantum gravity (BridgeQG) and CA21106 - COSMIC WISPers in the Dark Universe: Theory, astrophysics and experiments (CosmicWISPers).

Appendix A: Equatorial embeddings and spatial geometry

To provide a geometric visualization of the spatial curvature induced by the Kalb-Ramond-ModMax fields, we construct isometric embeddings of the equatorial plane ($\theta = \pi/2, t = \text{const.}$) into three-dimensional Euclidean space. Although such embeddings do not carry direct observational significance, they offer an intuitive representation of how the underlying spacetime geometry is deformed by the combined effects of Lorentz symmetry

breaking and nonlinear electrodynamics.

The induced two-dimensional metric on the equatorial slice is given by

$$d\sigma^2 = \frac{dr^2}{f(r)} + r^2 d\phi^2, \quad (\text{A1})$$

where $f(r)$ denotes the lapse function of the KR-ModMax black hole. This metric can be embedded in Euclidean space using the standard cylindrical parametrization $(r, \phi) \mapsto (r \cos \phi, r \sin \phi, z(r))$, where the embedding function $z(r)$ satisfies

$$\left(\frac{dz}{dr} \right)^2 = \frac{1}{f(r)} - 1. \quad (\text{A2})$$

Real solutions exist in regions where $f(r) < 1$, leading to the familiar funnel-shaped surfaces that encode the effective gravitational potential of the black hole.

In Fig. 12 we present representative equatorial embedding diagrams for four configurations belonging to the phantom ModMax branch. The surfaces extend outward from the event horizon radius r_+ (indicated by a black ring) and illustrate how spatial curvature accumulates as the horizon is approached. The vertical direction measures the embedding height $z(r)$, with steeper funnels corresponding to stronger curvature gradients. Superimposed blue spiral curves depict timelike geodesics of infalling test particles, included to visualize the qualitative motion of matter toward the horizon.

Several qualitative features can be identified. In Panel (a) ($\ell = 0.2, \gamma = 0.5, Q = 0.2, r_+ = 1.62$) we see a modest Kalb-Ramond deformation produces a wide, gently sloping funnel, indicative of a relatively weak curvature enhancement. In Panel (b) ($\ell = 0.5, \gamma = 3.0, Q = 0.5, r_+ = 1.02$) we observe a strong ModMax suppression ($e^{-\gamma} \ll 1$) yields a compact horizon and a sharply curved near-horizon geometry. In Panel (c) ($\ell = 0.7, \gamma = 1.0, Q = 0.8, r_+ = 1.24$) we can see a large Lorentz-symmetry-breaking parameter amplifies asymptotic deviations, producing pronounced geometric flattening away from the horizon. Finally, in Panel (d) ($\ell = 0.4, \gamma = 2.0, Q = 0.1, r_+ = 1.20$) we have a small electric charge with intermediate parameters illustrates the smooth transition toward the uncharged KR-Schwarzschild limit.

An important structural aspect revealed by these embeddings is the single-horizon topology of the phantom branch. In contrast to Reissner-Nordström-type geometries, no inner Cauchy horizon is present. As a result, the spacetime avoids the mass-inflation instability that typically afflicts charged black holes at the inner horizon. While a full dynamical stability analysis lies beyond the scope of this work, the absence of an inner horizon suggests that phantom KR-ModMax black holes may exhibit improved robustness against perturbations in the deep interior.

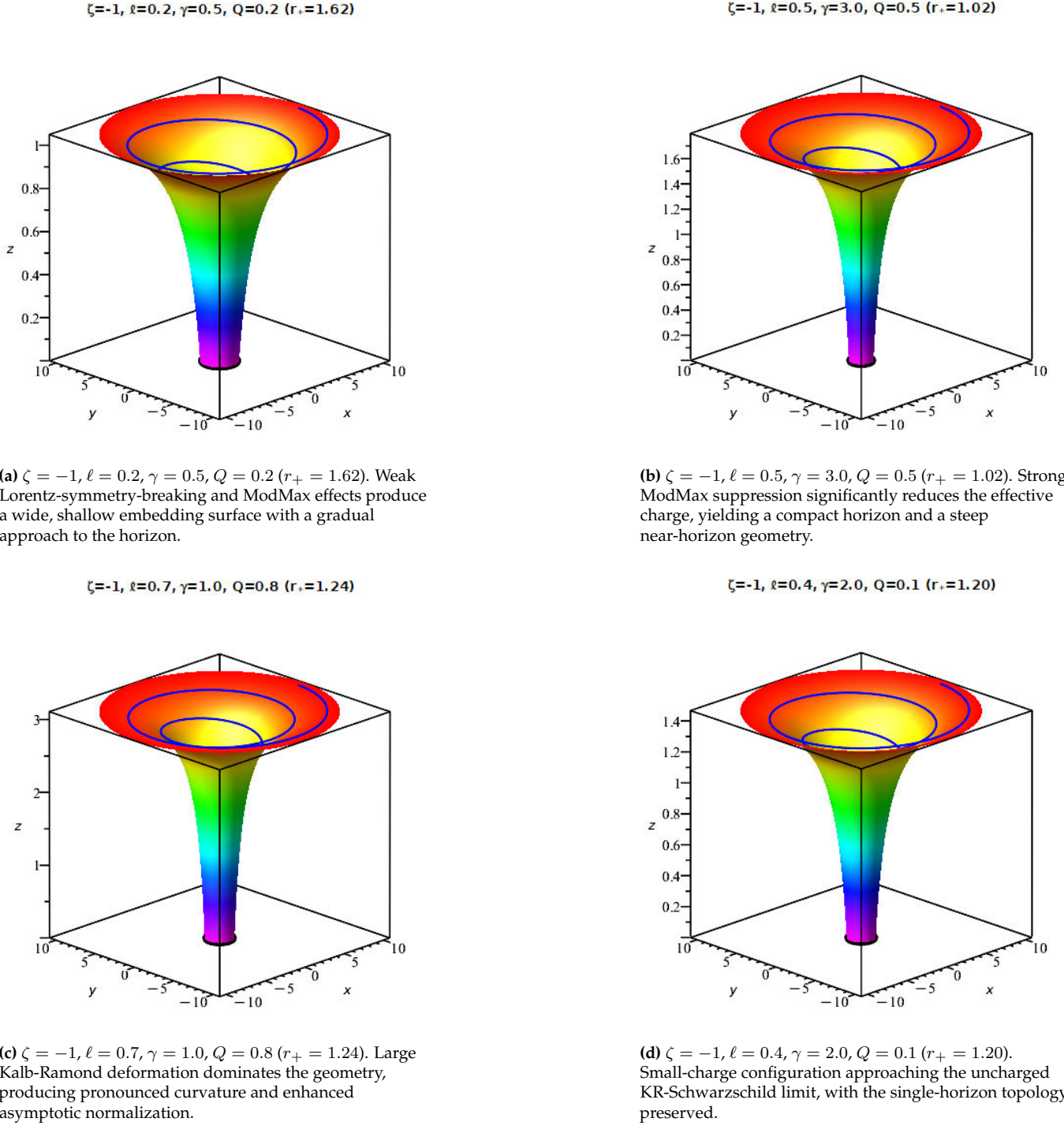


FIG. 12: Three-dimensional isometric embedding diagrams of the equatorial plane ($\theta = \pi/2, t = \text{const.}$) for phantom-branch ($\zeta = -1$) KR-ModMax black holes. Black rings mark the event-horizon radius $r = r_+$, while blue spirals represent timelike infalling trajectories. The depth and curvature of the embedding surface provide a geometric visualization of the combined effects of Lorentz symmetry breaking and nonlinear electrodynamics.

[1] Steven B. Giddings, “Black holes and other clues to the quantum structure of gravity,” *Galaxies* **9**, 16 (2021), [arXiv:2012.14434 \[gr-qc\]](https://arxiv.org/abs/2012.14434).

[2] Miguel Barroso Varela and Hugo Rauch, “Gravitational waves on charged black hole backgrounds in modified gravity,” *Gen. Rel. Grav.* **56**, 16 (2024), [arXiv:2311.07376](https://arxiv.org/abs/2311.07376)

[gr-qc].

[3] Emmanuel N. Saridakis *et al.* (CANTATA), *Modified Gravity and Cosmology. An Update by the CANTATA Network*, edited by Emmanuel N. Saridakis, Ruth Lazkoz, Vincenzo Salzano, Paulo Vargas Moniz, Salvatore Capozziello, Jose Beltrán Jiménez, Mariafelicia De Laurentis, and Gonzalo J. Olmo (Springer, 2021) [arXiv:2105.12582 \[gr-qc\]](https://arxiv.org/abs/2105.12582).

[4] Timothy Clifton, Pedro G Ferreira, Antonio Padilla, and Constantinos Skordis, “Modified gravity and cosmology,” *Physics reports* **513**, 1–189 (2012).

[5] Shin’ichi Nojiri and Sergei D. Odintsov, “Unified cosmic history in modified gravity: from F(R) theory to Lorentz non-invariant models,” *Phys. Rept.* **505**, 59–144 (2011), [arXiv:1011.0544 \[gr-qc\]](https://arxiv.org/abs/1011.0544).

[6] Cosimo Bambi, “Testing black hole candidates with electromagnetic radiation,” *Rev. Mod. Phys.* **89**, 025001 (2017), [arXiv:1509.03884 \[gr-qc\]](https://arxiv.org/abs/1509.03884).

[7] G. G. L. Nashed and Emmanuel N. Saridakis, “Rotating AdS black holes in Maxwell- $f(T)$ gravity,” *Class. Quant. Grav.* **36**, 135005 (2019), [arXiv:1811.03658 \[gr-qc\]](https://arxiv.org/abs/1811.03658).

[8] G. G. L. Nashed and Emmanuel N. Saridakis, “New rotating black holes in nonlinear Maxwell $f(\mathcal{R})$ gravity,” *Phys. Rev. D* **102**, 124072 (2020), [arXiv:2010.10422 \[gr-qc\]](https://arxiv.org/abs/2010.10422).

[9] G. G. L. Nashed and Emmanuel N. Saridakis, “Stability of motion and thermodynamics in charged black holes in $f(T)$ gravity,” *JCAP* **05**, 017 (2022), [arXiv:2111.06359 \[gr-qc\]](https://arxiv.org/abs/2111.06359).

[10] G. G. L. Nashed and Emmanuel N. Saridakis, “New anisotropic star solutions in mimetic gravity,” *Eur. Phys. J. Plus* **138**, 318 (2023), [arXiv:2206.12256 \[gr-qc\]](https://arxiv.org/abs/2206.12256).

[11] L. A. Lessa, J. E. G. Silva, R. V. Maluf, and C. A. S. Almeida, “Modified black hole solution with a background Kalb–Ramond field,” *Eur. Phys. J. C* **80**, 335 (2020), [arXiv:1911.10296 \[gr-qc\]](https://arxiv.org/abs/1911.10296).

[12] Zheng-Qiao Duan, Ju-Ying Zhao, and Ke Yang, “Electrically charged black holes in gravity with a background Kalb–Ramond field,” *Eur. Phys. J. C* **84**, 798 (2024), [arXiv:2310.13555 \[gr-qc\]](https://arxiv.org/abs/2310.13555).

[13] Erdem Sucu and Izzet Sakalli, “AdS black holes in einstein–kalb–ramond gravity: Quantum corrections, phase transitions, and orbital dynamics,” *NUCLEAR PHYSICS B* **1018** (2025), 10.1016/j.nuclphysb.2025.117081.

[14] Soumitra SenGupta and Saurabh Sur, “Spherically symmetric solutions of gravitational field equations in Kalb–Ramond background,” *Phys. Lett. B* **521**, 350–356 (2001), [arXiv:gr-qc/0102095](https://arxiv.org/abs/gr-qc/0102095).

[15] José Antonio Belinchón, “String-Inspired Gravity through Symmetries,” *Universe* **2**, 3 (2016).

[16] W. F. Kao, W. B. Dai, Shang-Yung Wang, Tzuu-Kang Chyi, and Shih-Yuun Lin, “Induced Einstein–Kalb–Ramond theory and the black hole,” *Phys. Rev. D* **53**, 2244–2247 (1996).

[17] Parthasarathi Majumdar and Soumitra SenGupta, “Parity violating gravitational coupling of electromagnetic fields,” *Class. Quant. Grav.* **16**, L89–L94 (1999), [arXiv:gr-qc/9906027](https://arxiv.org/abs/gr-qc/9906027).

[18] M. Born and L. Infeld, “Foundations of the new field theory,” *Proc. Roy. Soc. Lond. A* **144**, 425–451 (1934).

[19] Eloy Ayon-Beato and Alberto Garcia, “Regular black hole in general relativity coupled to nonlinear electrodynamics,” *Phys. Rev. Lett.* **80**, 5056–5059 (1998), [arXiv:gr-qc/9911046](https://arxiv.org/abs/gr-qc/9911046).

[20] Igor Bandos, Kurt Lechner, Dmitri Sorokin, and Paul K. Townsend, “A non-linear duality-invariant conformal extension of Maxwell’s equations,” *Phys. Rev. D* **102**, 121703 (2020), [arXiv:2007.09092 \[hep-th\]](https://arxiv.org/abs/2007.09092).

[21] Igor Bandos, Kurt Lechner, Dmitri Sorokin, and Paul K. Townsend, “On p-form gauge theories and their conformal limits,” *JHEP* **03**, 022 (2021), [arXiv:2012.09286 \[hep-th\]](https://arxiv.org/abs/2012.09286).

[22] Y. Sekhmani, S. K. Maurya, M. K. Jasim, İ. Sakalli, J. Rayimbaev, and I. Ibragimov, “Thermodynamics and phase transition of anti de Sitter black holes with ModMax nonlinear electrodynamics and perfect fluid dark matter,” *Eur. Phys. J. C* **85**, 229 (2025).

[23] B. Eslam Panah, B. Hazarika, and P. Phukon, “Thermodynamic Topology of Topological Black Hole in F(R)–ModMax Gravity’s Rainbow,” *PTEP* **2024**, 083E02 (2024), [arXiv:2405.20022 \[hep-th\]](https://arxiv.org/abs/2405.20022).

[24] V. Alan Kostelecký and Zonghao Li, “Gauge field theories with Lorentz-violating operators of arbitrary dimension,” *Phys. Rev. D* **99**, 056016 (2019), [arXiv:1812.11672 \[hep-ph\]](https://arxiv.org/abs/1812.11672).

[25] Erdem Sucu and İzzet Sakallı, “Exploring Lorentz-violating effects of Kalb–Ramond field on charged black hole thermodynamics and photon dynamics,” *Phys. Rev. D* **111**, 064049 (2025).

[26] Ke Yang, Yue-Zhe Chen, Zheng-Qiao Duan, and Ju-Ying Zhao, “Static and spherically symmetric black holes in gravity with a background Kalb–Ramond field,” *Phys. Rev. D* **108**, 124004 (2023), [arXiv:2308.06613 \[gr-qc\]](https://arxiv.org/abs/2308.06613).

[27] James M. Bardeen, B. Carter, and S. W. Hawking, “The Four laws of black hole mechanics,” *Commun. Math. Phys.* **31**, 161–170 (1973).

[28] S. W. Hawking, “Particle Creation by Black Holes,” *Commun. Math. Phys.* **43**, 199–220 (1975), [Erratum: *Commun. Math. Phys.* 46, 206 (1976)].

[29] Constantino Tsallis and Leonardo J. L. Cirto, “Black hole thermodynamical entropy,” *EUROPEAN PHYSICAL JOURNAL C* **73** (2013), 10.1140/epjc/s10052-013-2487-6.

[30] Constantino Tsallis, “Possible Generalization of Boltzmann–Gibbs Statistics,” *J. Statist. Phys.* **52**, 479–487 (1988).

[31] Emmanuel N. Saridakis, Kazuharu Bamba, R. Myrzakulov, and Fotios K. Anagnostopoulos, “Holographic dark energy through Tsallis entropy,” *JCAP* **12**, 012 (2018), [arXiv:1806.01301 \[gr-qc\]](https://arxiv.org/abs/1806.01301).

[32] Spyros Basilakos, Andreas Lymeris, Maria Petronikolou, and Emmanuel N. Saridakis, “Alleviating both H_0 and σ_8 tensions in Tsallis cosmology,” *Eur. Phys. J. C* **84**, 297 (2024), [arXiv:2308.01200 \[gr-qc\]](https://arxiv.org/abs/2308.01200).

[33] Everton M. C. Abreu and Jorge Ananias Neto, “Barrow black hole corrected-entropy model and Tsallis nonextensivity,” *Phys. Lett. B* **810**, 135805 (2020), [arXiv:2009.10133 \[gr-qc\]](https://arxiv.org/abs/2009.10133).

[34] Shin’ichi Nojiri, Sergei D. Odintsov, and Valerio Faraoni, “Generalized black hole entropy in two dimensions,” *Int. J. Geom. Meth. Mod. Phys.* **20**, 2350148 (2023), [arXiv:2303.02663 \[hep-th\]](https://arxiv.org/abs/2303.02663).

[35] Erdem Sucu, Izzet Sakalli, and Yusuf Sucu, “Spin dependent quantum corrections to schwarzschild black hole thermodynamics with barrow entropy and gup,” *International Journal of Geometric Methods in Modern Physics* (2026).

[36] S. I. Kruglov, “Magnetic black holes within Einstein–AdS gravity coupled to nonlinear electrodynamics, extended phase space thermodynamics and Joule–Thomson expansion,” *Can. J. Phys.* **101**, 739–748 (2023), [arXiv:2401.15115 \[physics.gen-ph\]](https://arxiv.org/abs/2401.15115).

[37] Jing Liang, Wei Lin, and Benrong Mu, “Joule–Thomson expansion of the torus-like black hole,” *Eur. Phys. J. Plus* **136**, 1169 (2021), [arXiv:2103.03119 \[gr-qc\]](https://arxiv.org/abs/2103.03119).

[38] İzzet Sakalli, Yusuf Sucu, and Erdem Sucu, “Zitterbewe-

gung oscillations and GUP-induced quantum modifications of Yang-Mills black holes in perfect fluid dark matter," *Nucl. Phys. B* **1022**, 117216 (2026).

[39] Meng-Yao Zhang, Hao Chen, Hassan Hassanabadi, Zheng-Wen Long, and Hui Yang, "Critical behavior and Joule-Thomson expansion of charged AdS black holes surrounded by exotic fluid with modified Chaplygin equation of state*," *Chin. Phys. C* **48**, 065101 (2024), [arXiv:2401.17589 \[gr-qc\]](#).

[40] F. W. Dyson, A. S. Eddington, and C. Davidson, "A Determination of the Deflection of Light by the Sun's Gravitational Field, from Observations Made at the Total Eclipse of May 29, 1919," *Phil. Trans. Roy. Soc. Lond. A* **220**, 291–333 (1920).

[41] Clifford M. Will, "The Confrontation between General Relativity and Experiment," *Living Rev. Rel.* **17**, 4 (2014), [arXiv:1403.7377 \[gr-qc\]](#).

[42] G. W. Gibbons and M. C. Werner, "Applications of the Gauss-Bonnet theorem to gravitational lensing," *Class. Quant. Grav.* **25**, 235009 (2008), [arXiv:0807.0854 \[gr-qc\]](#).

[43] M. C. Werner, "Gravitational lensing in the Kerr-Randers optical geometry," *Gen. Rel. Grav.* **44**, 3047–3057 (2012), [arXiv:1205.3876 \[gr-qc\]](#).

[44] Xin Ren, Yaqi Zhao, Emmanuel N. Saridakis, and Yi-Fu Cai, "Deflection angle and lensing signature of covariant f(T) gravity," *JCAP* **10**, 062 (2021), [arXiv:2105.04578 \[astro-ph.CO\]](#).

[45] Erdem Sucu and Ali Övgün, "The effect of quark-antiquark confinement on the deflection angle by the NED black hole," *Phys. Dark Univ.* **44**, 101446 (2024), [arXiv:2403.07044 \[gr-qc\]](#).

[46] Erdem Sucu, "Quantum gravity corrections and plasma-induced lensing of magnetically charged black holes," *Nucl. Phys. B* **1022**, 117285 (2026).

[47] Erdem Sucu and Izzet Sakalli, "Astrophysical reality of black hole thermodynamics and dynamics: Transformative influence of hernquist dark matter distributions," *PHYSICS OF THE DARK UNIVERSE* **49** (2025), 10.1016/j.dark.2025.102051.

[48] Qingqing Wang, Xin Ren, Yi-Fu Cai, Wentao Luo, and Emmanuel N. Saridakis, "Observational Test of f(Q) Gravity with Weak Gravitational Lensing," *Astrophys. J.* **974**, 7 (2024), [arXiv:2406.00242 \[astro-ph.CO\]](#).

[49] Volker Perlick, Oleg Yu. Tsupko, and Gennady S. Bisnovatyi-Kogan, "Influence of a plasma on the shadow of a spherically symmetric black hole," *Phys. Rev. D* **92**, 104031 (2015), [arXiv:1507.04217 \[gr-qc\]](#).

[50] Adam Rogers, "Frequency-dependent effects of gravitational lensing within plasma," *Mon. Not. Roy. Astron. Soc.* **451**, 17–25 (2015), [arXiv:1505.06790 \[gr-qc\]](#).

[51] Erdem Sucu, Izzet Sakalli, Özcan Sert, and Yusuf Sucu, "Quantum-corrected thermodynamics and plasma lensing in non-minimally coupled symmetric teleparallel black holes," *Phys. Dark Univ.* **50**, 102063 (2025), [arXiv:2508.11076 \[gr-qc\]](#).

[52] Michael Paul Hobson, George P Efstathiou, and Anthony N Lasenby, *General relativity: an introduction for physicists* (Cambridge university press, 2006).

[53] Peter Varga and Erik Grafarend, "Influence of tidal forces on the triggering of seismic events," *PURE AND APPLIED GEOPHYSICS* **175**, 1649–1657 (2018).

[54] Valeri Frolov and Igor Novikov, *Black hole physics: Basic concepts and new developments*, Vol. 96 (Springer Science & Business Media, 2012).

[55] Kevin B. Burdge *et al.*, "General relativistic orbital decay in a seven-minute-orbital-period eclipsing binary system," *Nature* **571**, 528–531 (2019), [arXiv:1907.11291 \[astro-ph.SR\]](#).

[56] Eric Poisson, "Tidal deformation of a slowly rotating black hole," *Phys. Rev. D* **91**, 044004 (2015), [arXiv:1411.4711 \[gr-qc\]](#).

[57] Y. Sekhmani, S. K. Maurya, J. Rayimbaev, M. Altanji, I. Ibragimov, and S. Muminov, "Lorentz-violating ModMax black holes in phantom-enhanced Kalb-Ramond gravity: Thermodynamics and topological charges," *Phys. Dark Univ.* **50**, 102079 (2025).

[58] Sergey Il'ich Kruglov, "AdS Black Holes in the Framework of Nonlinear Electrodynamics, Thermodynamics, and Joule-Thomson Expansion," *Symmetry* **14**, 1597 (2022), [arXiv:2209.05394 \[physics.gen-ph\]](#).

[59] Wentao Liu, Di Wu, and Jieci Wang, "Static neutral black holes in Kalb-Ramond gravity," *JCAP* **09**, 017 (2024), [arXiv:2406.13461 \[hep-th\]](#).

[60] Fabrizio Illuminati, Gaetano Lambiase, and Luciano Petrucciello, "Spontaneous Lorentz Violation from Infrared Gravity," *Symmetry* **13**, 1854 (2021), [arXiv:2108.09253 \[hep-th\]](#).

[61] Biswarup Mukhopadhyaya, Soumitra SenGupta, and Saurabh Sur, "Space-time torsion and parity violation: A Gauge invariant formulation," *Mod. Phys. Lett. A* **17**, 43–50 (2002), [arXiv:hep-th/0106236](#).

[62] H. Babaei-Aghbolagh, Komeil Babaei Velni, Davood Mahdavian Yekta, and H. Mohammadzadeh, "Manifestly SL(2, R) Duality-Symmetric Forms in ModMax Theory," *JHEP* **12**, 147 (2022), [arXiv:2210.13196 \[hep-th\]](#).

[63] Syed Masood, "The thermodynamic profile of AdS black holes in Lorentz-violating Bumblebee and Kalb-Ramond gravity," (2024), [arXiv:2411.06188 \[gr-qc\]](#).

[64] Robert M Wald, "Black hole entropy is the noether charge," *Physical Review D* **48**, R3427 (1993).

[65] G. W. Gibbons and R. E. Kallosh, "Topology, entropy and Witten index of dilaton black holes," *Phys. Rev. D* **51**, 2839–2862 (1995), [arXiv:hep-th/9407118](#).

[66] Stephen W Hawking, Gary T Horowitz, and Simon F Ross, "Entropy, area, and black hole pairs," *arXiv preprint gr-qc/9409013* (1994).

[67] Jacob D Bekenstein, "Black-hole thermodynamics," *Physics Today* **33**, 24–31 (1980).

[68] Tamás S. Biró and Viktor G. Czinner, "A q -parameter bound for particle spectra based on black hole thermodynamics with Rényi entropy," *Phys. Lett. B* **726**, 861–865 (2013), [arXiv:1309.4261 \[gr-qc\]](#).

[69] Ahmad Al-Badawi, Faizuddin Ahmed, and Izzet Sakalli, "Particle dynamics and thermal properties in Kalb-Ramond ModMax black holes: Theoretical predictions for observational tests of exotic physics," *Phys. Dark Univ.* **50**, 102076 (2025), [arXiv:2508.03226 \[gr-qc\]](#).

[70] David Kubiznak and Robert B. Mann, "P-V criticality of charged AdS black holes," *JHEP* **07**, 033 (2012), [arXiv:1205.0559 \[hep-th\]](#).

[71] M. Umair Shahzad and Lubna Nosheen, "Some remarks on criticality and thermodynamics of the dynamic phantom AdS black holes," *Eur. Phys. J. C* **82**, 470 (2022).

[72] Ekrem Aydin, Erdem Sucu, and Izzet Sakalli, "Regular magnetically charged black holes from nonlinear electrodynamics: Thermodynamics, light deflection, and orbital dynamics," *PHYSICS OF THE DARK UNIVERSE* **50** (2025), 10.1016/j.dark.2025.102164.

[73] Rui-Bo Wang, Lei You, Shi-Jie Ma, Jian-Bo Deng, and

Xian-Ru Hu, "Thermodynamic phase transition and Joule-Thomson expansion of a quantum corrected black hole in AdS spacetime," *Chin. Phys.* **49**, 115102 (2025), [arXiv:2504.06907 \[gr-qc\]](https://arxiv.org/abs/2504.06907).

[74] Vitor Cardoso and Paolo Pani, "Testing the nature of dark compact objects: a status report," *LIVING REVIEWS IN RELATIVITY* **22** (2019), 10.1007/s41114-019-0020-4.

[75] Sumanta Chakraborty and Soumitra SenGupta, "Strong gravitational lensing — A probe for extra dimensions and Kalb-Ramond field," *JCAP* **07**, 045 (2017), [arXiv:1611.06936 \[gr-qc\]](https://arxiv.org/abs/1611.06936).

[76] Mikko Partanen and Jukka Tulkki, "Light deflection in unified gravity and measurable deviation from general relativity in the second post-Newtonian order," (2025), [arXiv:2505.14446 \[gr-qc\]](https://arxiv.org/abs/2505.14446).

[77] Naoki Tsukamoto, Takao Kitamura, Koki Nakajima, and Hideki Asada, "Gravitational lensing in Tangherlini spacetime in the weak gravitational field and the strong gravitational field," *Phys. Rev. D* **90**, 064043 (2014), [arXiv:1402.6823 \[gr-qc\]](https://arxiv.org/abs/1402.6823).

[78] Erdem Sucu and İzzet Sakalli, "Scalar-tensor corrections and observational signatures of hairy black holes in horn-deski gravity," *HIGH ENERGY DENSITY PHYSICS* **56** (2025), 10.1016/j.hedp.2025.101220.

[79] Erdem Sucu and İzzet Sakalli, "Quantum-corrected thermodynamics and plasma lensing of MOG black holes," *Proc. Roy. Soc. Lond. A* **481**, 20250251 (2025).

[80] MA ABRAMOWICZ, B CARTER, and JP LASOTA, "Optical reference geometry for stationary and static dynamics," *GENERAL RELATIVITY AND GRAVITATION* **20**, 1173–1183 (1988).

[81] Volker Perlick, "Fermat principle in Finsler spacetimes," *Gen. Rel. Grav.* **38**, 365–380 (2006), [arXiv:gr-qc/0508029](https://arxiv.org/abs/gr-qc/0508029).

[82] Shao Wen Wei, Yu Xiao Liu, and Chun E. Fu, "Null Geodesics and Gravitational Lensing in a Nonsingular Spacetime," *Adv. High Energy Phys.* **2015**, 454217 (2015), [arXiv:1510.02560 \[gr-qc\]](https://arxiv.org/abs/1510.02560).

[83] Erdem Sucu and İzzet Sakalli, "Charged regular black holes in quantum gravity: from thermodynamic stability to observational phenomena," *Eur. Phys. J. C* **85**, 989 (2025).

[84] R. Epstein and I. I. Shapiro, "POST POSTNEWTONIAN DEFLECTION OF LIGHT BY THE SUN," *Phys. Rev. D* **22**, 2947–2949 (1980).

[85] Steven Weinberg, *Gravitation and cosmology: principles and applications of the general theory of relativity* (John Wiley & Sons, 2013).

[86] Avery Broderick and Abraham Loeb, "Imaging the Black Hole Silhouette of M87: Implications for Jet Formation and Black Hole Spin," *Astrophys. J.* **697**, 1164–1179 (2009), [arXiv:0812.0366 \[astro-ph\]](https://arxiv.org/abs/0812.0366).

[87] Kazunori Akiyama *et al.* (Event Horizon Telescope), "First M87 Event Horizon Telescope Results. V. Physical Origin of the Asymmetric Ring," *Astrophys. J. Lett.* **875**, L5 (2019), [arXiv:1906.11242 \[astro-ph.GA\]](https://arxiv.org/abs/1906.11242).

[88] Gabriel Crisnejo and Emanuel Gallo, "Weak lensing in a plasma medium and gravitational deflection of massive particles using the Gauss-Bonnet theorem. A unified treatment," *Phys. Rev. D* **97**, 124016 (2018), [arXiv:1804.05473 \[gr-qc\]](https://arxiv.org/abs/1804.05473).

[89] Daniela S. J. Cordeiro, Ednaldo L. B. Junior, José Tar-ciso S. S. Junior, Francisco S. N. Lobo, Manuel E. Ro-drígues, Diego Rubiera-García, Luís F. Dias da Silva, and Henrique A. Vieira, "Free-falling test particles in a charged Kalb-Ramond black hole: Gravitational Doppler effect and tidal forces," *Phys. Rev. D* **112**, 104018 (2025), [arXiv:2503.12048 \[gr-qc\]](https://arxiv.org/abs/2503.12048).

[90] Subrahmanyan Chandrasekhar, *The mathematical theory of black holes* (1985).

[91] Eric Poisson, *A relativist's toolkit: the mathematics of black-hole mechanics* (Cambridge university press, 2004).